

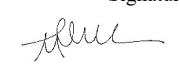


Christine Nims

**Exploring the impact of silica and divalent cations on microbial iron respiration and secondary mineral products in Archean ocean simulations**

Submitted in partial fulfillment of the requirements for the degree of  
**Master of Science in Earth and Environmental Sciences**  
Department of Earth and Environmental Sciences  
The University of Michigan

 _____ Signature	Accepted by: <b>Jena E. Johnson</b> _____ Name	<b>Jul. 23, 2021</b> _____ Date
 _____ Signature	<b>Gregory J. Dick</b> _____ Name	<b>August 3, 2021</b> _____ Date
 _____ Department Chair Signature	<b>Marin K. Clark</b> _____ Name	<b>August 18, 2021</b> _____ Date

I hereby grant the University of Michigan, its heirs and assigns, the non-exclusive right to reproduce and distribute single copies of my thesis, in whole or in part, in any format. I represent and warrant to the University of Michigan that the thesis is an original work, does not infringe or violate any rights of others, and that I make these grants as the sole owner of the rights to my thesis. I understand that I will not receive royalties for any reproduction of this thesis.

- Permission granted.
- Permission granted to copy after: \_\_\_\_\_
- Permission declined.

\_\_\_\_\_  
Author Signature



# Exploring the impact of silica and divalent cations on microbial iron respiration and secondary mineral products in Archean ocean simulations

Christine Nims  
University of Michigan

## ABSTRACT

Widespread chemical sedimentary deposits known as Banded Iron Formations (BIFs) archive Archean ocean chemistry and, potentially, traces of ancient microbial life. Microbial Fe(III) respiration likely influenced the mineralization of early BIF sediments. One hypothesis suggests that the early diagenetic bioreduction of primary iron oxides in BIFs resulted in the formation of other iron phases, including iron-rich silicates, carbonates, and magnetite common in BIF assemblages. Here, we simulated this proposed pathway in experimental/laboratory incubations of *Shewanella putrefaciens* CN32, a model iron-reducing bacterium, grown under conditions mimicking the predicted Archean seawater geochemistry. We examined the variability in the secondary mineral precipitates that formed in the presence or absence of calcium, magnesium, and dissolved silica to assess the impact of silica and divalent cations on the resultant mineral product. We analyzed the reduced mineral phases harvested from these experiments using Raman spectroscopy, electron microscopy, powder x-ray diffraction, and spectrophotometric techniques to identify mineral precipitates and track the distributions of  $\text{Fe}^{2+}/\text{Fe}^{3+}$ . We detected a diverse range of calcium carbonate morphologies and polymorphism in incubations with calcium. We also identified aggregates of wavy, iron- and silica-rich, amorphous precipitates in all DIR incubations amended with silica. Our observations indicate that microbial iron reduction of ferrihydrite is a viable pathway for precursor iron silicate phases. This finding allows us to draw parallels between our experimental proto-silicates and the iron silicate nano-inclusions in BIF chert deposits, suggesting that early iron silicates could be signatures of iron-reducing metabolisms on early Earth.

## INTRODUCTION

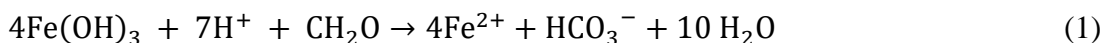
Precambrian Banded Iron Formations (BIFs) are extensive iron- and silica-rich chemical sedimentary deposits that precipitated from anoxic, ferruginous seawater throughout the Archean Eon and Paleoproterozoic Era (Klein, 2005; Bekker *et al.*, 2010; Farquhar *et al.*, 2010; Poulton & Canfeld, 2011; Johnson & Molnar, 2019). BIFs are often interpreted as distinctive archives of Archean marine biogeochemical cycling, where water column precipitates may have captured the intersection of ancient biological activity and seawater chemistry (Konhauser *et al.*, 2017). The accurate identification of the primary BIF deposit precipitates—and any evidence of early diagenetic reworking—is critical to reconstructing ancient seawater chemistry and deciphering the potential impact of microbial life on BIF formation, particularly in the absence of a robust fossil record (Knoll *et al.*, 2016).

However, the complex and micron-scale BIF mineral assemblage often precludes the discrimination of early BIF mineral component(s). BIFs contain iron oxides (magnetite ( $\text{Fe}_3\text{O}_4$ ) and hematite ( $\text{Fe}_2\text{O}_3$ )), iron silicates (greenalite ( $(\text{Fe})_3\text{Si}_2\text{O}_5(\text{OH})_4$ ), riebeckite, and stilpnomelane), microcrystalline quartz ( $\text{SiO}_2$ , also known as chert), and carbonates (siderite ( $\text{FeCO}_3$ ), dolomite ( $\text{CaMg}(\text{CO}_3)_2$ ), ankerite ( $\text{Ca}(\text{Fe}^{2+},\text{Mg})(\text{CO}_3)_2$ ) (Trendall, 2002; Klein, 2005;

Bekker *et al.*, 2013). While ferric (Fe(III) hydroxides, Fe(OH)<sub>3</sub>) are widely hypothesized to be the initial BIF precipitate (e.g., Konhauser *et al.*, 2017), much of the BIF assemblage likely derived from post-depositional processes including microbial respiration (Konhauser *et al.*, 2005; Heimann *et al.*, 2010; Craddock & Dauphas, 2011), fluid-mediated reactions (Sun *et al.*, 2015a), various grades of metamorphism (Trendall, 2002; Krapež *et al.*, 2003; Klein, 2005; Bekker *et al.*, 2013), and oxidizing fluids (Rasmussen *et al.*, 2013, 2014). Despite efforts to distinguish the imprint of post-depositional processes on BIF mineral formation, the depositional environment, precursor phases, and the role of biology in BIF genesis remain disputed (Johnson *et al.*, 2013; Konhauser *et al.*, 2017; Tosca *et al.*, 2019; Rasmussen *et al.*, 2021).

In an effort to resolve the initial BIF mineral, high-resolution petrographic studies recently observed early-forming iron silicate nanoparticle inclusions in well-preserved 2.4 to 3.5 billion-year-old South African and Australian BIF cherts (Rasmussen *et al.*, 2015b; Muhling & Rasmussen, 2020; Rasmussen *et al.*, 2021). Ubiquitous early-mineralizing chert in BIFs is often attributed to the estimated high dissolved silica concentrations in the Archean ocean (Siever, 1992), which was absent of silica-secreting organisms (Maliva *et al.*, 2005). The early diagenetic cementation of low porosity chert (Krapež *et al.*, 2003; Fischer & Knoll, 2009) makes it exemplary for the preservation of original minerals, textures (Rasmussen *et al.*, 2015a), and microfossils (Maliva *et al.*, 2005; Knoll *et al.*, 2016). Therefore, the discovery of widespread and abundant greenalite nanoinclusions in BIF cherts points to greenalite as an original seawater precipitate (Rasmussen *et al.*, 2016, 2019, 2021; Muhling & Rasmussen, 2020).

However, another proposed mechanism for the precipitation of early iron silicate minerals is through the microbial respiration of iron oxides in BIF sediments in the presence of high dissolved silica (Walker, 1984; Fischer & Knoll, 2009; Percak-Dennet *et al.*, 2011; Robbins *et al.*, 2019). Indeed, the preserved iron clay inclusions in BIF cherts contain 10-20 % Fe<sup>3+</sup> (Johnson *et al.*, 2018), which could represent relict Fe(III) originating from initial iron oxide minerals reduced through post-depositional iron respiration (Johnson *et al.*, 2018; Johnson, 2019). Dissimilatory iron reduction (DIR) is an anaerobic respiratory metabolism, performed by a variety of microbes, coupling the oxidation of organic carbon with the reduction of Fe(III) substrates (Lovley *et al.*, 1988; Myers & Nealson, 1990; Miot & Etique, 2016; Kato *et al.*, 2019) (see Equation 1, using CH<sub>2</sub>O as the simplified source of organic carbon).



This paired iron- and carbon-cycling metabolism has been suggested as both the progenitor of iron formation carbonates, where Fe(II)CO<sub>3</sub> precipitated from porewaters saturated in Fe(II) and inorganic carbon, and as an explanation for the exhausted supplies of organic carbon in Precambrian BIFs (Walker, 1984; Baur *et al.*, 1985; Konhauser *et al.*, 2005; Johnson *et al.*, 2008; Heimann *et al.*, 2010; Craddock & Dauphas, 2011). Likewise, microbial iron respiration in the high silica Archean seawater could have produced secondary iron silicate biominerals, as proposed by Fischer and Knoll (2009), with the saturation of Fe(II) and dissolved silica.

Extensive DIR research details the diversity of secondary mineral products that form in microbial iron respiration incubations. Existing research catalogs the impact of wide-ranging electron donor selection (Fredrickson *et al.*, 2003; Salas *et al.*, 2009; O'Loughlin *et al.*, 2019), bacterial species and strain (O'Loughlin *et al.*, 2007; Salas *et al.*, 2010), and cell density (Zegeye *et al.*, 2010) on DIR biomineral precipitates. Other studies document the interaction of oxyanions

( $\text{SO}_4^{2-}$ ,  $\text{PO}_4^{3-}$ ) and electron shuttles (Zegeye *et al.*, 2005; Zachara *et al.*, 2011; Bae & Lee, 2013), effects of Fe concentrations (Piepenbrock *et al.*, 2011), the significance of released/soluble biogenic Fe(II) (Han *et al.*, 2018), and the effects of various iron substrates (Langley *et al.*, 2009; Etique *et al.*, 2016) in DIR-driven secondary mineralization. While this prior DIR work displays the spectrum of DIR-mediated mineral products, ranging from secondary Fe(III) oxides to Fe(II,III) phases, such as magnetite or the Fe(II,III) green rust salt, the absence of dissolved silica in these studies decouples their mineral observations from predictions of ancient DIR products in the siliceous geochemistry of Archean seawater.

A limited set of experimental and environmental DIR studies examine the effect of silica on iron respiration. These studies investigate the reduction of structural Fe(III) within smectite or illite phases (Kostka *et al.*, 1996, 1999; O'Reilly, 2005; Stucki & Kostka, 2006; Furukawa & Reilly, 2007; Komlos *et al.*, 2007; Dong *et al.*, 2009), the bioreduction of FeOOH-coated quartz sands (Sergent *et al.*, 2011; Yahaya *et al.*, 2019), microbial iron reduction in silicifying hot spring settings (Phoenix *et al.*, 2003), and electron transfer with periplasmic nanowires (Gorby *et al.*, 2006). Many of these silica-amended DIR experiments use organic buffers, i.e. PIPES (Kukkadapu *et al.*, 2004; Zachara *et al.*, 2011), phosphate buffers (Komlos *et al.*, 2007), artificial electron shuttles, i.e. anthraquinone-2, 6- disulfonate (AQDS) (Yahaya, Sergent), or chelators, i.e. ethylenediaminetetraacetic acid (EDTA) (O'Reilly, 2005; Furukawa & Reilly, 2007; Koo *et al.*, 2016), making these experimental results less suitable for comparison to the Archean environment.

This prior work identified amorphous silica globules (Furukawa & Reilly, 2007), biogenic illite (Koo *et al.*, 2016), magnetite (Kukkadapu *et al.*, 2004; Sergent *et al.*, 2011; Li *et al.*, 2013b); iron carbonates, siderite (O'Reilly, 2005) and chukanovite (Sergent *et al.*, 2011); carbonate green rust (Kukkadapu *et al.*, 2004); and vivianite or ferrous phosphates (Kukkadapu *et al.*, 2004; Peretyazhko *et al.*, 2010) as secondary mineral products. Komlos *et al.* (2007) did detect putative secondary Fe(II) silicates by Mössbauer spectroscopy but used aluminosilicate mineralized clay as a starting iron substrate. Irrespective of this range of explored experimental conditions, no study has heretofore demonstrated the formation of authigenic Fe(II)-iron silicates as a secondary mineral product of Fe(III) oxide respiration.

Research investigating DIR in simulated ancient marine conditions remains limited. Archean-relevant DIR work focused on the Fe isotopic signals during Fe(III) oxide respiration in the presence of dissolved silica (Wu *et al.*, 2009) and during respiration of Si-Fe(III) gels (Percak-Dennet *et al.*, 2011), as well as the implications of DIR of Si-Fe(III) gels on Si isotope fractionation (Reddy *et al.*, 2016). However, these isotope-centered studies did not characterize the secondary mineral products from DIR of Fe(III)-Si gels in artificial Archean seawater, with the exception of a singular, putative smectite mineral (Percak-Dennet *et al.*, 2011). However, this tentative three-layered phase is distinct from the two-layer greenalite minerals hosted in BIF cherts and was not analyzed further.

In addition, the experimental solutions do not entirely reflect the pH values or ionic composition of seawater constrained by Archean-Paleoproterozoic models. Ancient seawater composition varied from the experimental conditions employed in the vast majority of DIR studies. Recent models suggest the Archean ocean had ( $[\text{Si}_{\text{aq}}] = 0.67$  to 2 mM (Konhauser *et al.*, 2007; Jones *et al.*, 2015), a circumneutral pH of 6.5-7.5 (Jones *et al.*, 2015; Halevy & Bachan, 2017; Krissansen-Totton *et al.*, 2018) and approximate concentrations of 10 mM dissolved inorganic carbon (DIC) ca. 2.5 Ga (Halevy & Bachan, 2017). Generally, calcium [ $\text{Ca}^{2+}$ ] estimates in Archean seawater are analogous to the modern ocean concentration of 10 mM

(Holland, 1984; Higgins *et al.*, 2009), though other recent estimates suggest higher [Ca<sup>2+</sup>] concentrations of at 35-40 mM (Jones *et al.*, 2015) or 50-100 mM (Halevy & Bachan, 2017). The prior Archean-like DIR studies were completed at an elevated pH of 8.7 (Wu *et al.*, 2009) or high DIC/bicarbonate concentrations ( $\geq 30$  mM) (Percak-Dennet *et al.*, 2011; Reddy *et al.*, 2016). In contrast, other Archean-relevant experiments focused on characterizing DIR-promoted Ca/Fe-carbonate precipitation (Zeng & Tice, 2014) and did not incorporate dissolved silica in the experimental matrix. Thus, a more extensive biomineral evaluation of DIR products in simulated Archean seawater, with high levels of silica, is essential to understanding whether DIR could be responsible for the genesis of early iron silicate minerals in BIFs.

In this study, we use batch experiments to examine the secondary phases that form after microbial iron reduction, as performed by a model iron reducing bacterium, with synthesized ferrihydrite as the electron acceptor and lactate as the electron donor across a range of chemistries. Specifically, we tested the impact of dissolved silica and divalent cations (i.e. calcium and magnesium), on the microbial reduction of ferrihydrite in conditions representative of Archean marine environments. Our thorough characterization of DIR secondary mineral precipitates and analysis of solution chemistry reveals how the interplay of iron, dissolved silica, and divalent cations can alter the products of microbial iron respiration, including the formation of potential precursor iron silicates.

## METHODS

### *Preparation of Shewanella putrefaciens cell suspensions*

Frozen stocks of *Shewanella putrefaciens* CN32 (ATCC strain BAA-453) stored at -80 °C in 25% glycerol were revived in tryptic soy broth (TSB) (Bacto Tryptic Soy Broth, BD) at room temperature in a shaking incubator at 150 rpm. Cells were harvested after 24 hours by centrifugation (5 min x 2,000 x g) in sterile epi tubes. We washed cell slurries three times in a 0.22  $\mu$ m filter-sterilized salt solution composed of 400 mM NaCl, 10 mM KCl, 1 mM NH<sub>4</sub>Cl to remove organic residues from the TSB broth. Rinsed cell stocks were dispensed into a sterile serum and re-suspended with 180 mL of the sterile rinsing salt solution (~3% inoculum). This suspension was sparged with filter-sterilized (Millex, 0.22  $\mu$ m PVDF membrane) N<sub>2</sub> gas (99.9%) for 10 minutes at 5-6 PSI to prepare the cell stock for addition to anoxic experiments. The optical density (OD) of the inoculum cell suspension was 0.337 at 600 nm (Genesys 50 UV-Vis spectrophotometer, Thermo Fisher).

### *Preparation of the artificial Archean seawater (AAS) medium*

Autoclaved ultra-pure Milli-Q water in borosilicate bottles was boiled (90°C) and purged with filter-sterilized (Millex filters, 0.22  $\mu$ m PVDF membrane) N<sub>2</sub> (99.9%) to remove dissolved oxygen. The solution was stoppered and transferred into an anoxic glovebox (MBraun, 99.9% N<sub>2</sub>). Subsequently, the water was stirred for 48 hours in the glovebox system, partially capped to prevent contamination during the removal of residual oxygen.

The artificial seawater medium (AAS), adapted from Hinz *et al.* (2021), Reddy *et al.* (2016), and Percak-Dennet *et al.* (2011), was modified with lower concentrations of bicarbonate, magnesium, and ammonium to mimic the conditions and ion concentrations constrained by

models of Neoproterozoic ocean geochemistry (Jones *et al.*, 2015; Halevy & Bachan, 2017; Krissansen-Totton *et al.*, 2018). Phosphate was entirely excluded from the medium to preclude the precipitation of insoluble iron phosphates (Fredrickson *et al.*, 1998; Jorand *et al.*, 2000) not observed in the rock record. The final basal medium contained the following: 400 mM NaCl, 9 mM KCl, 1 mM NH<sub>4</sub>Cl, which was buffered by 10 mM NaHCO<sub>3</sub> and supplemented with amino acids (glutamine, serine, and alanine, 20 μg mL<sup>-1</sup>, (Myers & Nealson, 1990)), 1 mL L<sup>-1</sup> SL-10 trace minerals (Widdel *et al.*, 1983) and 1 mL L<sup>-1</sup> vitamin solution (Balch & Wolfe, 1976). The medium was additionally augmented with 30 mM sodium lactate (NaC<sub>3</sub>H<sub>5</sub>O<sub>3</sub>) as the electron donor, in excess of [Fe(III)], to prevent any electron donor limitation in the microbial reduction experiments.

Solid NaCl, KCl, and NH<sub>4</sub>Cl salts were first fully dissolved in previously prepared anoxic water. The bicarbonate stock solution was subsequently added to the medium to a final concentration of 10 mM, and the medium was titrated with anoxic 3 M HCl to a pH of 7. The lactate, amino acid, trace mineral, and vitamin solutions were then individually dispensed into the medium under constant mixing in the glovebox. After mixing, this basal AAS medium was subdivided into two solutions with and without 1 mM dissolved silica dispensed from anoxic and filtered sodium metasilicate stock (Na<sub>2</sub>SiO<sub>3</sub>, Sigma Aldrich). The medium was then partitioned into 8 separate autoclaved 250 mL Kimax bottles to test the effects of each cation in the presence and absence of silica: 10 mM CaCl<sub>2</sub>, 10 mM MgCl<sub>2</sub>, 10 mM MgCl<sub>2</sub> and 10 mM CaCl<sub>2</sub> combined, and a condition without added cations. These divalent cations were added from a filtered stock solution of calcium, magnesium, or both, while maintaining the pH at 7. All solutions were sealed with sterile black rubber stoppers in the anoxic glovebox, wrapped in aluminum foil, and stored at 4°C prior to experimental setup.

#### *Synthesis of ferrihydrite substrate*

We synthesized a ferrihydrite substrate using a method adapted from Sklute *et al.* (2018). A solution of 0.5 M ferric chloride (FeCl<sub>3</sub>) was slowly neutralized with NaOH to a thick slurry with a final pH of 7. The ferrihydrite substrate then ripened for 30 minutes with slow mixing (150 rpm) and a final pH measurement was taken to verify a constant circumneutral value (pH of 7). The ferrihydrite was rinsed twice by centrifugation (5,000 x g) in ultrapure Milli-Q water to remove excess salts but prevent transformation to hematite. The ferrihydrite was stored in aluminum-wrapped sterile falcon tubes at 4°C prior to use in experiments. The Ferrozine assay was used on small subsets of the ferrihydrite to calculate the total iron concentration of the initial ferrihydrite stock dispensed into experimental vessels (see Ferrozine section for details). Raman spectroscopy confirmed that we successfully synthesized ferrihydrite (see Fig. S1).

#### *Experimental Procedure*

Ferrihydrite was dispensed on the benchtop to a final concentration of 1.5 mM into 80 mL autoclaved serum bottles loosely capped with sterile foil. All serum bottles containing ferrihydrite were transferred into the anoxic glovebox and allowed to equilibrate with the N<sub>2</sub> headspace. Prepared AAS solutions were brought to room temperature and placed in the glovebox. After 35 mL of specific batch medium was pipetted into each respective serum bottle containing ferrihydrite, the bottles were sealed with a butyl stopper and aluminum crimp. On the

benchtop, we added 5 mL of the *S. putrefaciens* cell suspension (12.5% inoculum) for a final volume of 40 mL. All incubations ran in triplicate with an abiotic control at each condition. The serum bottles were placed in dark incubator at 31°C, within the optimal growth temperatures for *S. putrefaciens* CN32 (Pakchung *et al.*, 2008) to maximize reduction. The bottles were lightly agitated manually twice a month to homogenize solution conditions and ensure full precipitate exposure for a total experimental duration of 19 weeks.

### *Mineral harvest and characterization*

At the end of the bioreduction experiment, samples of the solid precipitates and aliquots of solutions from each condition were harvested in the glovebox. Final pH was measured upon the disassembly of each serum (see Fig. S2). Solids were extracted from each replicate, centrifuged in sterile epitubes, and rinsed three times in anoxic, ultrapure water. All solid and solution samples were stored in Epitubes and individually sealed in Mylar bags in an N<sub>2</sub> atmosphere and were transferred into a -80°C freezer for preservation until analysis.

For scanning electron microscopy (SEM) analyses, pre-rinsed precipitates were thawed and dispensed (15 µL) onto carbon tape atop aluminum stubs and allowed to dry in the glovebox. Dried samples were immediately transported to a vacuum coater (Denton Desk II) and sputtered with Au for 100s. Secondary electron images of mineral precipitates were collected using a JEOL JSM-7800FLV SEM system operating at an accelerating voltage of 10-15 kV and a working distance of 10 mm. Qualitative elemental maps and spectra using energy dispersive spectroscopy (EDS) were obtained using an Oxford XMaxN 80mm<sup>2</sup> silicon-drift energy-dispersive X-ray spectrometer. Spectra were processed using Oxford Aztec v3.3 software.

Transmission electron microscopy (TEM) analyses were conducted on representative subsamples of each experimental condition. For TEM preparation, mineral residues were thawed in the anaerobic chamber and re-suspended in anoxic Milli-Q water in preparation. A 5 µL droplet of sample was pipetted onto 300-mesh carbon-coated lacey formvar Cu grid (Ted Pella). After drying, the grids were individually stored in holders sealed in Mylar pouches during transport to the Michigan Center for Materials Characterization (MC<sup>2</sup>) facility. The TEM grids were only exposed to oxygen in the transition between the loading of the grid onto the holder and the insertion of the holder under vacuum in the microscope column. S/TEM imaging and analysis used an FEI Talos F200X G2 S/TEM system equipped with a Gatan OneView 4K camera, operating at an accelerating voltage of 200 kV. The morphology and elemental chemistry of nano- and micro-scale mineral precipitates were characterized by bright-field TEM and high-angle annular dark-field (HAADF) STEM imaging respectively. Qualitative EDS spectra were collected with a Super-X window-less detector and processed with the Velox platform. Selected area electron diffraction (SAED) patterns and high-resolution TEM (HRTEM) imaging enabled the mineral identification of imaged particles. Fast Fourier-transforms (FFTs) of lattice fringes captured in HRTEM images facilitated the determination of mineral d-spacing. All bright-field, HRTEM images, and SAED patterns were analyzed using Gatan Digital Micrograph software.

For Raman analyses, pre-rinsed precipitates thawed to 25°C were suspended in anoxic Milli-Q water in the anaerobic chamber. Small volumes (25 µL) of sample were pipetted onto designated aluminum foil-wrapped glass microscope slides to diminish the background signal of glass when

measured with a 785 nm excitation source. Mineral residues dried for approximately 1 hour in the anaerobic chamber. Individual slides were successively removed from the anaerobic chamber for Raman analysis to avoid prolonged exposure to oxygen prior to analysis. Raman microspectroscopy measurements were taken on a Horiba XploRA PLUS Raman spectrometer/system paired with an Olympus BX41 microscope. Spectra were collected using a laser excitation of 785 nm. The 785 nm diode excitation laser was selected for these samples based on the resonant Raman effect of the 532 nm laser with c-type cytochromes, common membrane proteins in the *S. putrefaciens*. Spectra were collected using a groove density of 1200 gr/mm over a range of 150 – 1200  $\text{cm}^{-1}$  to examine the specific spectral features of calcium carbonate mineral polymorphs at 10 mW laser power. Scans were obtained using a 50x long working distance objective with an integration time of 10 seconds and 15 accumulations. Polynomial baseline correction was used to remove background fluorescence in the LabSpec6 platform. The standards for calcite (#R040070) and aragonite (#R040078) are sourced from the RRUFF database. Raman analysis was performed under ambient conditions.

For Powder X-ray Diffraction (XRD) analysis, rinsed precipitates were pipetted into Kapton tubes that were heat-sealed in the anaerobic chamber. Kapton tubes stored in individual Mylar bags ( $\text{N}_2$  headspace) were shipped to the McMaster Analytical X-Ray Diffraction Facility (MAX) in Ontario, Canada for analysis. 2D XRD data was collected using a Bruker D8 DISCOVER with Vantec500 area detector equipped with a  $\text{Cu K}\alpha$  source. Samples were analyzed using 4 frames per scan for either 20- or 60-minute scans, and scans were collected using a default bisection scan geometry with an omega rotation for each frame with a  $10^\circ$  width. Samples were measured in reflection mode with a zero background silicon wafer in several orientations and areas along the Kapton tube. Background subtraction on raw files limited the fluorescence produced by iron minerals and signal from the Kapton tube. 2D frames were integrated into 1D plots using DIFFRAC.EVA software (v5.1, Bruker AXS). Diffraction patterns were plotted in OriginPro and compared with mineral standards obtained from the RRUFF database.

### *Solution chemistry*

Fe(II)/Fe(III) speciation and total Fe concentration of post-incubation solutions, control solutions, and solids were determined using the Ferrozine assay (Stookey, 1970; Viollier *et al.*, 2000). Incubated solution and rinsed biomineral precipitates were collected from two separate replicates for Ferrozine measurements. In addition, each condition control was sampled in duplicate to measure its iron concentrations and redox speciation in solutions and solids. Before addition to batch experiments, a subsample of the starting ferrihydrite substrate, digested in 6 M HCl, was also analyzed by Ferrozine to confirm redox state and estimate starting Fe(III) concentration.

Aliquots of the solutions and solids were first diluted with 0.5 M HCl and 3 M HCl, respectively, and reacted for 30 minutes in the anaerobic chamber. After acidification, Ferrozine colorimetric analysis performed with a UV-Vis spectrophotometer (Genesys 50 UV-Vis spectrophotometer) operated at 562 nm following Viollier *et al.* (2000).

## **RESULTS**



## Solution chemistry

### pH

All experiments initiated at a pH of  $7 \pm .05$ . After the 19-week incubation, we found that the pH of all experiments increased an average of  $\sim 0.7$  compared to pre-incubation pH measurements (Fig. S2). Siliceous experiments concluded with slightly higher pHs.

### Partitioning of Fe

Overall, Ferrozine measurements demonstrated the strong effect of silica on the partitioning of microbially-liberated aqueous Fe(II). We observed a higher total measured Fe(II) in the final solutions of inoculated experiments without dissolved silica, averaging  $\sim 0.2$  mM higher relative to their silica-containing counterparts (Fig. 1A; Supplemental Table 1). In silica-deficient conditions, experiments with calcium or magnesium cations demonstrated even higher aqueous [Fe(II)] compared to the samples without these divalent cations (AAS-only). The combined cation experiment without silica had  $\sim 5x$  total soluble iron (mean [Fe(II)] = 0.50 mM) than the total Fe(II) present in the AAS-only samples (mean [Fe(II)] = 0.11 mM).

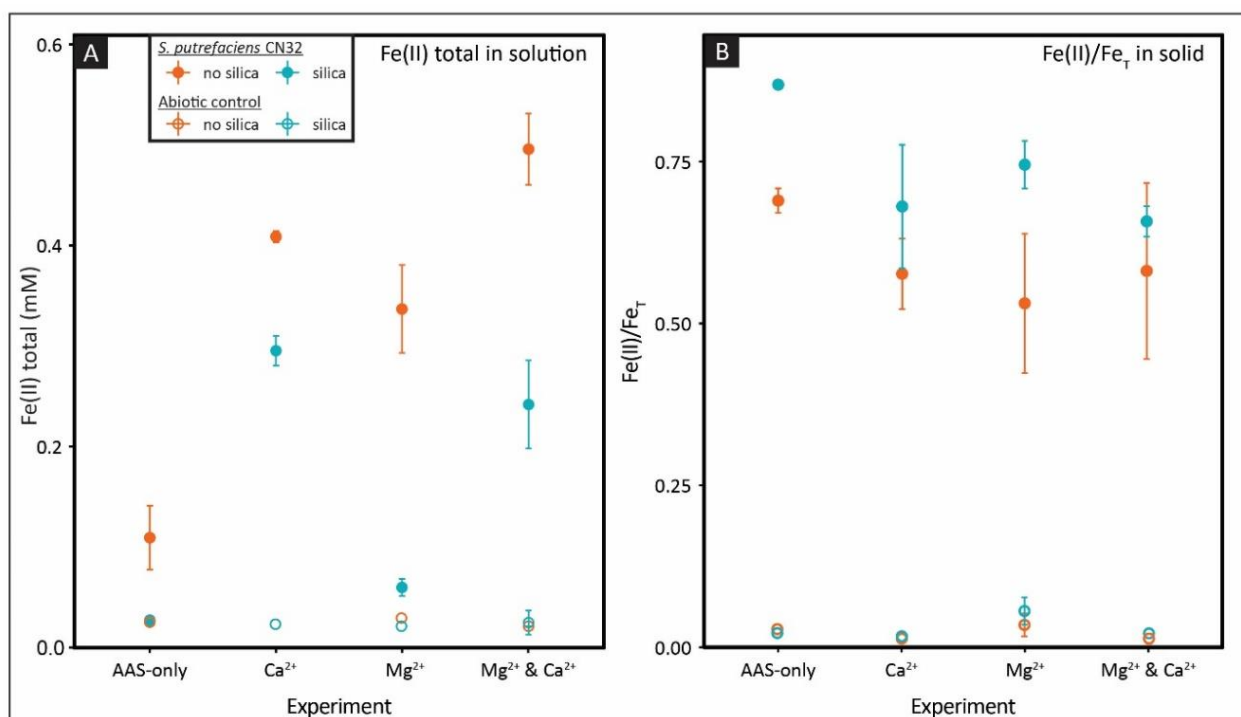


Figure 1: Ferrozine measurements of aqueous Fe(II) (A) and the Fe(II)/Fe<sub>total</sub> ratio of solid precipitates (B) in both inoculated experiments and controls. Data points represent means and error bars indicate one standard deviation.

While all silica-augmented experiments had lower Fe(II) total in solution, the magnesium- and magnesium-calcium supplemented conditions had considerably lower soluble iron than their counterpart lacking silica (Fig. 1). Magnesium-bearing inoculated experiments without silica had mean final ferrous iron concentrations ([Fe(II)] = 0.34 mM), which decreased in the presence of silica ([Fe(II)] = 0.06). The combined cation experiment with silica had nearly 50% less ferrous iron in solution ([Fe(II)] = 0.24 mM, compared to 0.50 mM Fe(II) without Si).

Notably, the calcium-supplemented solutions had the highest ferrous iron concentration of all of the siliceous experiments ( $[\text{Fe(II)}] = 0.30 \text{ mM}$ ), a value proximal to the ferrous concentration in the calcium solution without silica ( $[\text{Fe(II)}] = 0.41$ ) (Supplemental, Table 1).

Conversely, in experiments supplemented with silica, solid precipitates contained higher proportions of Fe(II) relative to the total measured iron. All bioreduced siliceous solids presented higher Fe(II)/T ratios (Fig. 1B). The magnesium-augmented and AAS-only with silica experiments demonstrated particularly elevated Fe(II)/T (0.87 and 0.74) in precipitates compared to the solids in their silica-deficient counterpart experiments (0.69 and 0.53).

The mean aqueous Fe(II) in abiotic control solutions ranged from 0.02 to 0.03 mM, similar to the baseline levels of ferrous iron observed by Reddy *et al.* (2016). In control solutions, aqueous  $[\text{Fe(II)}]$  did not vary in the presence or absence of silica.

## **X-ray diffraction**

Bulk XRD measurements on solids from *S. putrefaciens* incubations primarily produced either characteristic patterns of the calcium carbonate polymorphs, calcite and aragonite, or no definitive features/peaks (Fig. 2). Diffractograms of both the AAS-only and magnesium-amended condition, in the presence and absence of silica, showed no detectable crystalline mineral phases (Fig. 2). XRD profiles of incubations with added magnesium or calcium, however, demonstrated peaks indicative of calcite and aragonite. While we tentatively identified the magnetite (400) peak in the combined cation experiment with silica, we did not detect any other diagnostic magnetite peaks in these measurements. We identified the primary calcite peak (104) in the calcium-amended incubation, regardless of silica content (Fig. 2).

*S. putrefaciens* incubations supplemented with magnesium and calcium presented no significant peaks in silica-free experiments, but peaks of both calcite and aragonite in the silica-amended conditions. We performed Raman spectral analysis on the magnesium- and calcium-amended incubation lacking silica given its low signal XRD profile, and indeed verified the presence of both Ca-carbonate polymorphs in this combined cation experiment. Therefore, we investigated each incubation using TEM-SAED and Raman spectroscopy techniques, to fully characterize the nano-crystalline and microscale minerals that formed in these bioreduction experiments.

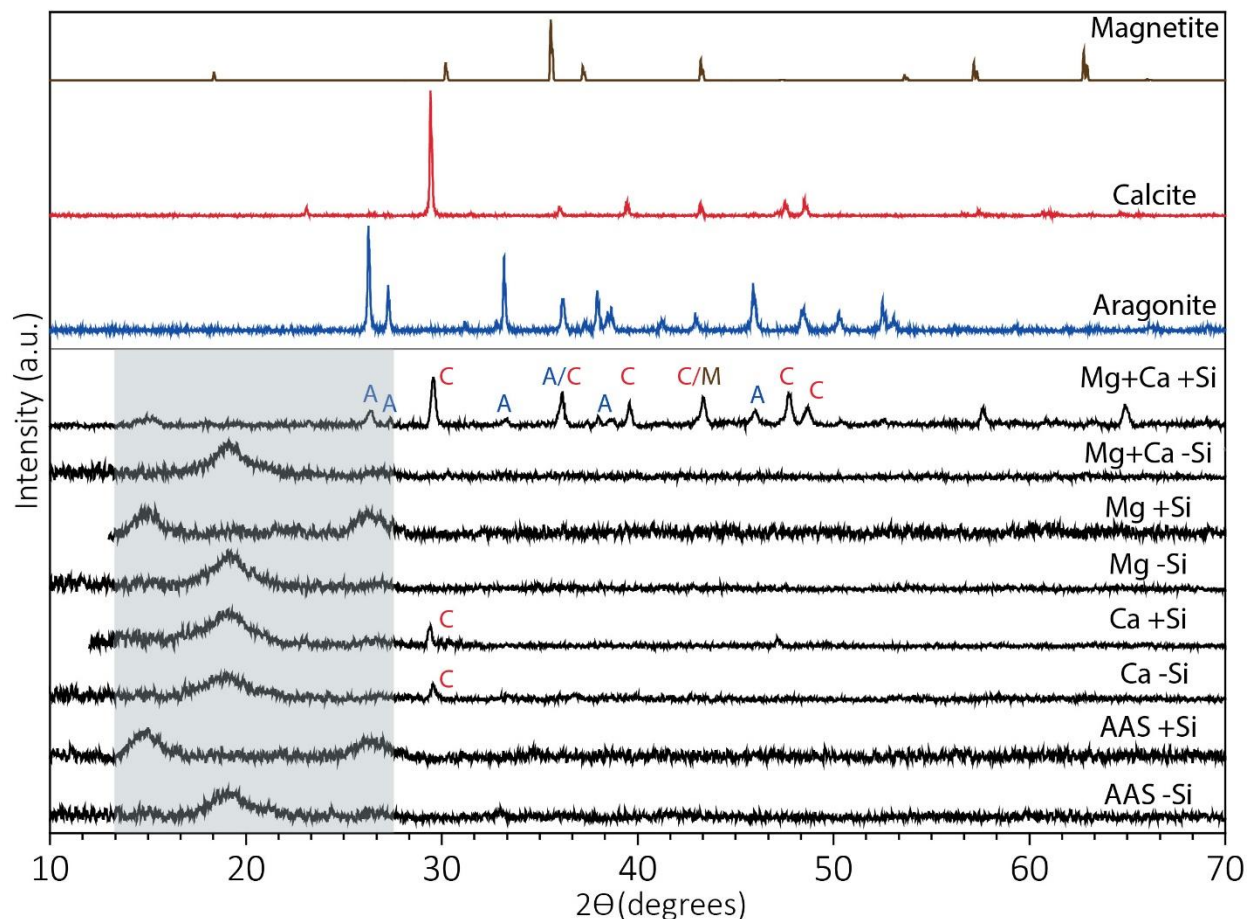


Figure 2: XRD patterns showing bulk measurements of different mineralogy by condition in 19-week incubations of *S. putrefaciens*. The peaks are labeled as A for aragonite, C for calcite, M and for magnetite. The grayed region represents background signal from the Kapton tube. Diffractogram standards for magnetite, calcite, and aragonite plotted above experimental patterns for reference.

## Characterization of experiments

### Abiotic control experiments

Control serum bottles without *S. putrefaciens* consisted of unaltered ferrihydrite after 19 weeks. TEM images and EDS mapping showed widespread iron- and oxygen-rich aggregates of ~5 nm pseudo-hexagons characteristic of two-line ferrihydrite (2LFh, (Janney *et al.*, 2000)) in samples without silica (Fig. S3 A,B,C), with silica (Fig. S3 D,E,F), and with silica, calcium, and magnesium (Fig. S3 G,H). XRD measurements showed no discernable peaks. The precipitates appeared to be either amorphous by FFT of an HRTEM image (S3 E inset) and/or composed of 2LFh by the distinctive rings (~2.5 Å and 1.5 Å) in an electron diffraction pattern of another sample (Fig. S3 G, inset). We detected low concentrations of silica in some EDS measurements of the AAS-only control (~2-3 at. %) (Fig. S3 F), which could be linked to leaching of the borosilicate glass after 19 weeks.

### Calcium- and Magnesium-Free Artificial Archean Seawater (AAS) incubations

AAS-only incubations after 19 weeks of *S. putrefaciens* grown on ferrihydrite and lactate without silica contained Fe-rich crusts intermixed with biomass or extracellular polymeric

substances (EPS). We found microbial biofilms with adsorbed iron in these experiments, contrary to the separated mineral precipitates that formed in the other cation-containing conditions. SEM imaging revealed spherical indentations distributed across portions of the crust (Fig. 3A) and nano-scale chains of 5-10 nm globular precipitates entrained in biomass (Fig. 3B). Our TEM/STEM images resolved cells containing 50 to 100 nm laths embedded in the periplasm and/or adsorbed to the cellular surface (Fig. 3C,D,E,G). We identified these laths as lepidocrocite, or  $\gamma$ -FeOOH, by the characteristic 6.2 Å spacing parallel to the elongated axis and high Fe content (Fig. 3G). This lepidocrocite appeared intimately associated with either cell surfaces (Fig. 3D) or an organic-rich matrix (Fig. 3E).

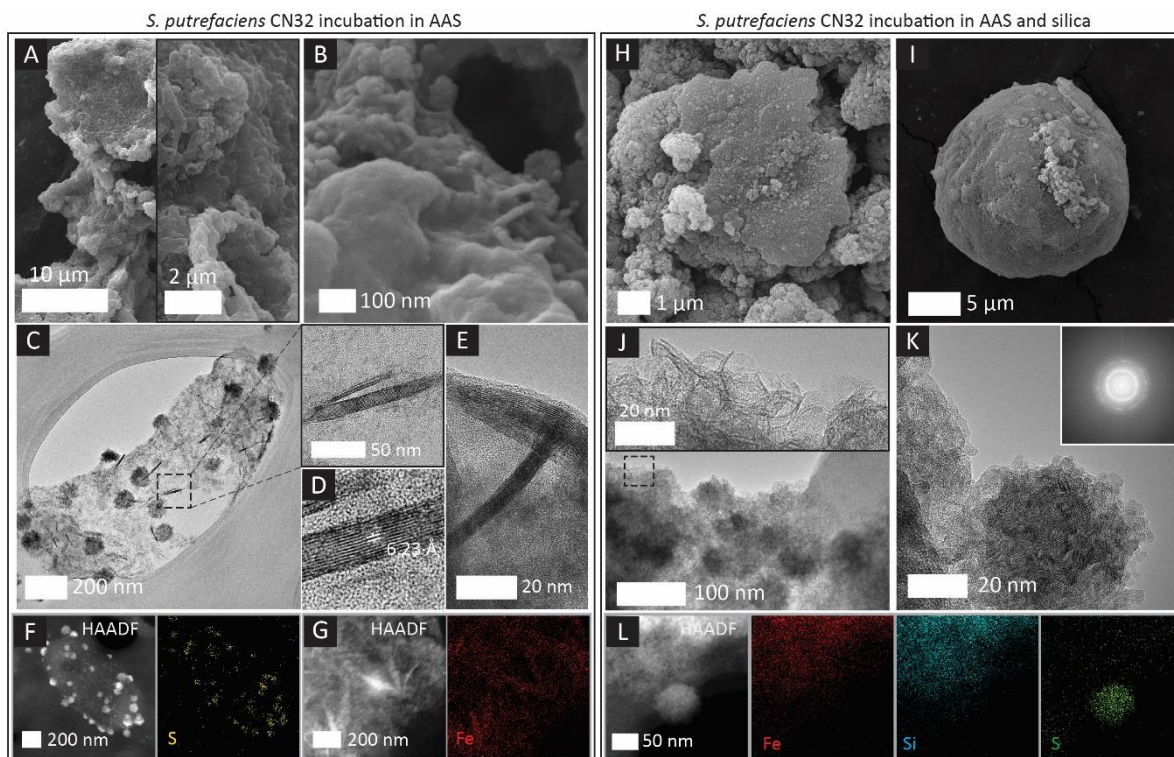


**Figure 3:** Electron imaging and elemental maps of biomineral precipitates in calcium- and magnesium-free experiments. Cohesive iron crusts (A), embedded nanochain morphologies (B); *S. putrefaciens* cells presenting lepidocrocite laths embedded in the cellular membrane (C) with a higher resolution subset; HRTEM of the characteristic 6.2 Å (200) interplanar spacing of lepidocrocite (D); elongated laths of  $\gamma$ -FeOOH in an organic film (E); STEM-HAADF and corresponding EDS mapping of membrane-associated sulfur-rich granules in yellow (F) and embedded intracellular lepidocrocite, with iron shown in red (G). SEM images of the silica-amended experiment showed irregular crusts (H) and spherical morphologies (I); TEM images of amorphous, wavy features interspersed with globular structures (J) and FFT of an HRTEM image shows the globules are polycrystalline; STEM-EDS mapping of a similar area shows an iron- and silica-rich matrix (L) with adjoined sulfur granules (green).

Additionally, we detected 50-100 nm sulfur-rich granules associated with the cellular membranes of AAS-only *S. putrefaciens* in HAADF images and TEM-EDS maps (Fig. 3C,F). The solution medium was absent of sulfur constituents and the amino acids in the AAS medium (alanine, glutamine, and serine) lack sulfur groups that could be sources of sulfur. We suspect that the *S. putrefaciens* inoculum, derived from rinsed TSB stock cultures, likely retained some

residual sulfur-rich compounds from the rich medium, perhaps in cellular stores of sulfur, which served as the sulfur source for these granules.

AAS-only incubations augmented with silica produced similar iron crusts (Fig. 1H) and larger-scale (~10  $\mu\text{m}$ , Fig. 3I) spherical aggregates. This experimental condition produced a silica- and iron-rich coprecipitate matrix, composed of thin, platy particles lacking diffracting domains or identifiable fringes (Fig. 3J,L). The curling, poorly layered structures of this Fe-Si phase were distinct from the starting 2LFh substrate with adsorbed silica (Fig. S1) that instead showed 2-4 nm pseudo-hexagonal crystallites with poorly defined lattice fringes. These siliceous AAS-only precipitates also contained 50 nm sulfur-rich granules similar to their silica-free counterparts; however, the sulfur minerals, perceptible as dark, round features in Figure 3 I,J,K, were interspersed in iron- and silica-rich precipitates. In the presence of silica, the sulfur granules did not appear closely affiliated with discrete cells, although it is possible that dense siliceous aggregates obscured this association. FFT of an HRTEM image of the sulfur grains (Fig. 3K inset) indicated polycrystalline grains, and STEM-EDS mapping highlights the notable deficiency of iron, ruling out the precipitation of iron sulfide minerals (Fig. 3L).

#### *Calcium-augmented incubations*

Supplemented with calcium, *S. putrefaciens* CN32 incubations produced large (10-50  $\mu\text{m}$ ) calcium carbonate minerals and secondary iron oxyhydroxide minerals. In experiments with calcium but lacking dissolved silica, we observed the precipitation of abundant calcium carbonate minerals but no evidence of iron-rich carbonates (such as siderite or ankerite). SEM images demonstrated the broad variety of Ca-carbonate minerals and morphologies, from stacks of blocky calcite with acicular aragonite overgrowths (Fig. 4A) to large rhombohedral calcite crystals featuring irregular surfaces (Fig. 4B). SEM-EDS maps highlighted the separation between iron and calcium carbonate phases, with carbonates forming alongside deposits of iron-rich precipitates (Fig. 4D). Raman analysis of spindle-like and euhedral carbonate minerals (Fig. 4G) in calcium-amended experiments produced distinctive spectral features of aragonite and calcite respectively, validating the identity of calcium-rich particles evident in SEM imaging but too sizeable for TEM analysis (Fig. 4H). SEM imaging and TEM-based analyses of the iron-rich precipitates revealed aggregates of 10-20 nm acicular needles (Fig. 4C, E). The SAED pattern of these needles showed strong lattice reflections for goethite or  $\alpha$ -FeOOH (1.44, 1.70, 2.19, and 2.48  $\text{\AA}$ ) (Fig. 4E, subset). A 2.48  $\text{\AA}$  d-spacing obtained from FFT of the lattice fringe of an individual needle (Fig. 4F) was also consistent with goethite.

Silica-supplemented incubations with calcium yielded extensive calcium carbonate precipitation immersed in a siliceous iron matrix (Fig. 4I). Calcite euhedra presented step defects (Fig. 4J) and occasionally a veneer of iron-silica nano-colloids (Fig. 4J,K). TEM analysis showed a dense bundle of crystallites (Fig. 4L,M,N) enriched in calcium, associated with aggregates of iron and silica (Fig. 3O). FFT collected from the HRTEM image of this crystallite bundle (Fig. 4M, subset) exhibited a nanograin lattice fringe with an inter-planar distance consistent with the (200) reflection of aragonite (Fig. 4N). Raman measurements of precipitates harvested from the *S. putrefaciens* incubations with added calcium and silica showed an abundance of both calcite and aragonite (Fig. 4Q). In several instances, we observed iron-tinted calcite minerals alongside pristine, unaltered aragonite in optical micrographs collected during Raman analysis (Fig. 4Q).

In these incubations with calcium and silica, we also identified amorphous, wavy iron- and silica-rich precipitates. These morphologies were similar to the AAS-only experiment, albeit

with aggregates forming rounded morphologies in HAADF images (Fig. 4P). These aggregates were low in calcium (1 at. %), but high in silica (24 at. %) and iron (19 at. %) (Fig. 4P). An SAED pattern of this siliceous deposit showed faint characteristic reflections of residual 2LFh from the starting substrate (Fig. 4R).

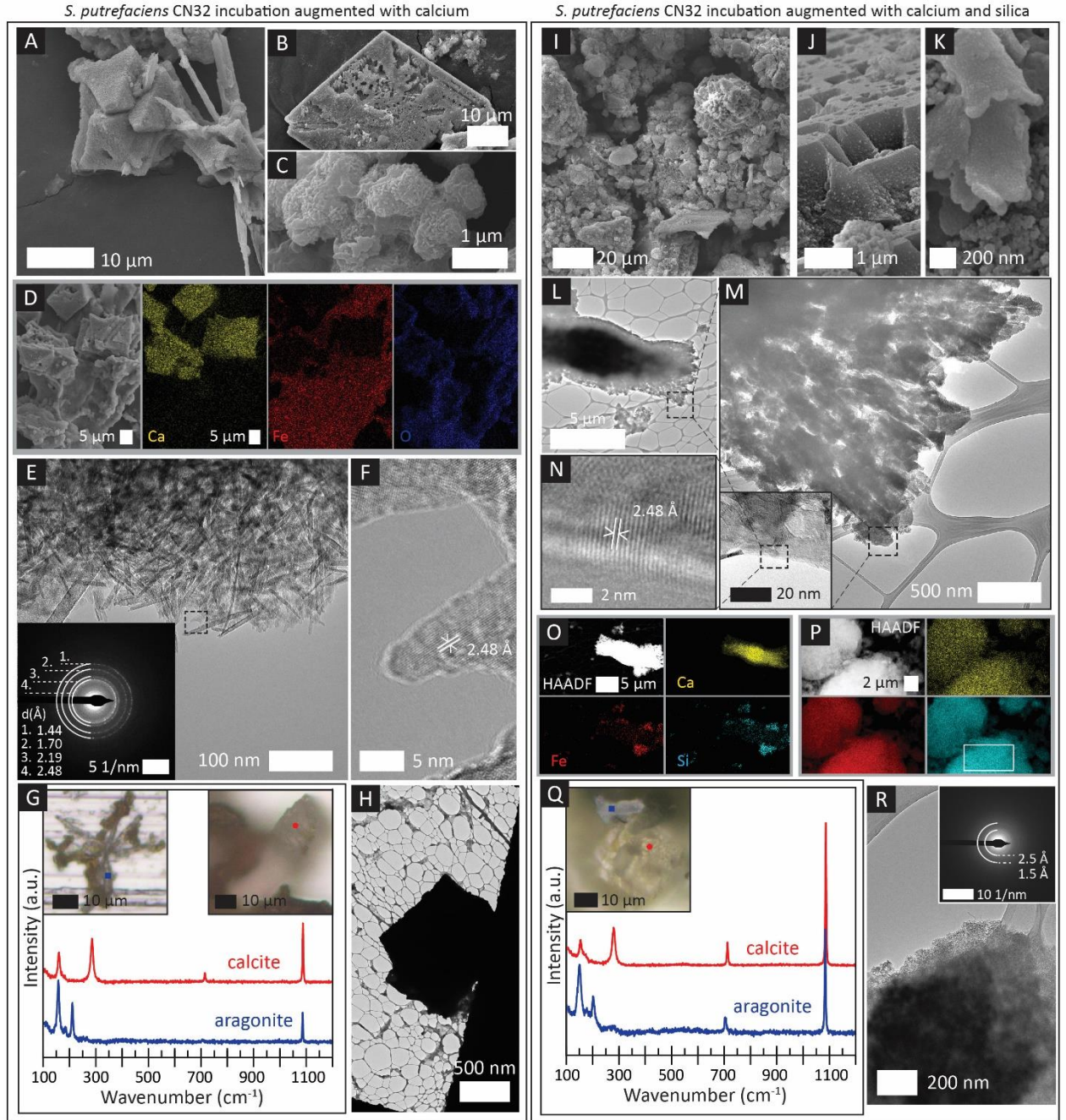


Figure 4: Characterization of biominerals formed in *S. putrefaciens* incubations amended with calcium. Large calcium carbonates (A,B), clusters of iron-rich rod-like minerals (C); elemental maps of biomineral precipitates calcium in yellow, iron in red, and oxygen in dark blue (D); TEM image of  $\alpha$ -FeOOH needles (E) with SAED inset showing reflections characteristic of goethite; HRTEM image of an individual needle displaying the characteristic 2.5 Å (111) spacing of goethite (F); Raman spectra of calcite (red) and aragonite (blue) minerals paired with corresponding images of scan locations demarcated in the same color scheme without silica (G) and with silica (Q);

large euhedral calcite imaged with low resolution TEM (H); SEM images of carbonates comingled with Fe-Si coprecipitates in experiments with added silica (I); carbonates (J) and iron minerals (K) presenting a nano-colloidal coating; TEM image of a bundle of calcium carbonates (L), analyzed at higher resolution (M); FFT of HRTEM images of a polycrystalline edge (M, inset) indicate the 2.5 Å d-value of aragonite (200) (N); STEM-HAADF and corresponding EDS maps show the elemental distribution of calcium, iron, and silica (cyan) in the bundle of carbonate crystallites from (L-M) and rounded discs of iron- and silica-rich coprecipitates, low in calcium (P); rectangle in (P) details location of EDS data collection; TEM image of an Fe-Si aggregate similar to the precipitates mapped in (P) composed of amorphous phases and some residual 2LFh (R).

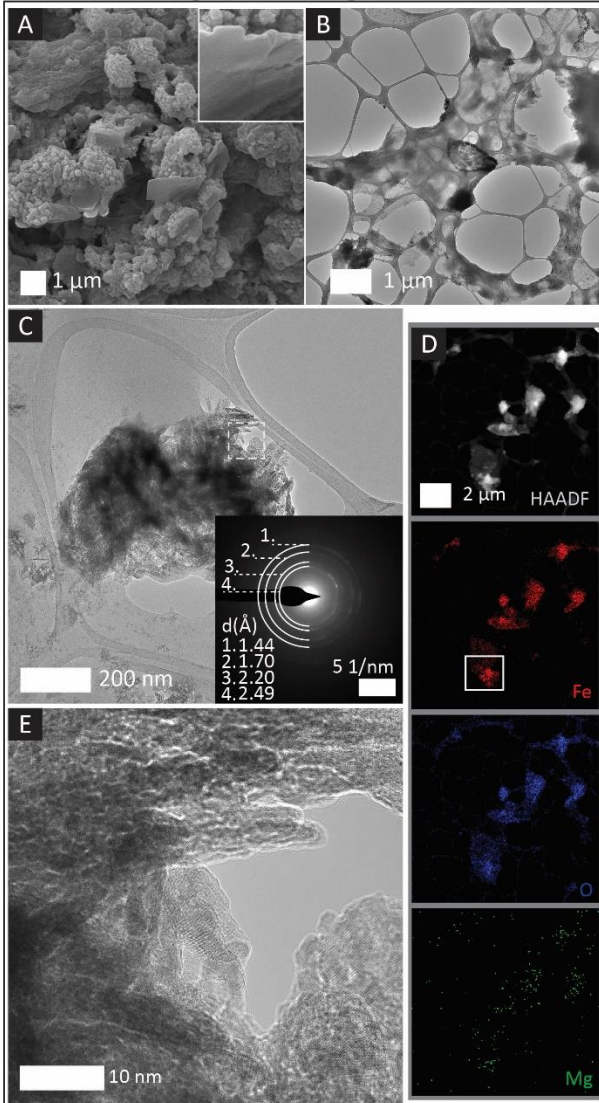
### Magnesium-augmented incubations

In incubations of *S. putrefaciens* supplemented with magnesium but without silica present, we observed the precipitation of iron-rich nanogranules and occasional plate-like minerals. These plates had smooth, notched edges (Fig. 5A, inset) and were composed of iron (25 at. %), carbon (56 at. %) and oxygen (16 at. %). Based on the close association with cellular textures in SEM images (Fig. 5A, B), we hypothesize that biomass provided a matrix for iron minerals, possibly remnant 2LFh, secondary FeOOH, or putative laths of chukanovite ( $\text{Fe}_2(\text{CO}_3)(\text{OH})_2$ ), in the magnesium experiment (Fig. 5A, B). Higher resolution TEM imaging of the crusts revealed aggregates of rod-shaped particles (Fig. 5C) containing a high percentage of Fe (18 at. %) and limited magnesium incorporation (<1 at. %) (Fig. 5D). HRTEM of these particles showed rods with sub-angular facets compared to the acicular goethite identified in Figure 3E. Overlapping crystallites indicated an inter-planar spacing consistent with goethite (2.6 Å (210)) (Fig. 5E), however, the less defined rods could be composed of six-line ferrihydrite (6LFh) which shares some coincident inter-planar spacings with  $\alpha$ -FeOOH. The SAED pattern of the same aggregate presented soft/smear reflections (Fig. 5C, subset) in lieu of similar reflections of discrete spots (Fig. 4E, subset). This distinction, combined with the sub-angular facets, could suggest a possible mixture of goethite and 6LFh.

In silica-rich incubations amended with magnesium, large cohesive masses of iron and silica-rich granules dominated biomineral precipitates. We observed 5-10 µm globular structures (Fig. 5F) intermixed with unstructured crusts and planar deposits (Fig. 5G) with SEM. TEM imaging revealed aggregates consisting of homogeneous, curling cellophane-like particles (Fig. 5H), similar to the siliceous AAS-only and calcium-amended Fe-Si precipitates. HRTEM imaging underscored structures with fragile folded layers (Fig. 5H, subset), while FFT analysis demonstrated the amorphous composition of these phases (Fig. 5H, subset). EDS spectra/mapping indicated that the structures consisted of 24 at. % Si, 27 at. % Fe, and 2 at. % Mg. An SAED pattern of a large sheet of folded phases also contained diffuse reflections of 2LFh (1.5 and ~2.5 Å) (Fig. 5J), suggesting that the wavy structures form in association with the 2LFh substrate. HAADF images and STEM-EDS also revealed sparse hexagonal phases (Fig. 5I) with similar atomic percentages relative to the surrounding matrix of folded precipitates. However, thick layers of overlying wavy phases/Fe-Si aggregate could mask elemental or crystalline distinctions in HAADF images or diffraction of the sparse hexagonal inclusions.

Additionally, STEM-EDS mapping showed *S. putrefaciens* membranes enriched in sulfur (6 at. %). Distinct from the more isolated sulfur-rich granules associated with the cellular membranes of AAS-only *S. putrefaciens* (Fig. 2C,F), sulfur was uniformly distributed across cell membranes in the magnesium-amended incubation (Fig. S4).

SCN 32 incubation augmented with magnesium



SCN 32 incubation augmented with magnesium and silica

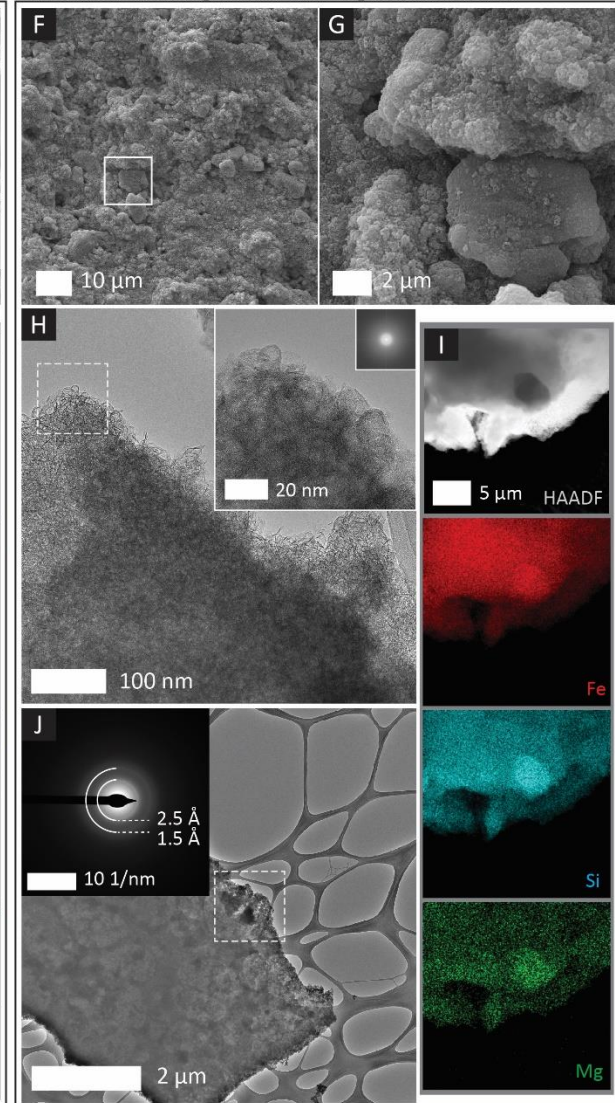


[Figure 5: Images and analysis of biominerals formed in *S. putrefaciens* incubations amended with magnesium. SEM images of granular iron crusts containing biomass and planar features (A) and TEM images of a network of organic/EPS webbing (B); TEM of rounded goethite minerals (C) and SAED (inset) showing characteristic reflections of goethite, and possibly 6LFh; STEM-EDS maps of rod aggregates (D), with elemental data collected from area designated with white rectangle; HRTEM of overlapping rods (E) imaged from dashed area in (C); SEM images of silica-amended globular forms (F) revealing more mineralized phases embedded in a matrix at higher magnification (G); TEM image of folding, curling layers (H) and HRTEM of edge region enclosed in white dashed box; FFT of this HRTEM shows these wavy phases are indeed amorphous (H, minor subset); STEM-EDS analysis of a similar mass of Fe-Si rich-precipitates shows high enrichment in iron and silica, with EDS measured from the area enclosed in white (I); SAED of these aggregates shows faint 2LFh reflections (J).]

### Calcium- and magnesium-augmented incubations

In silica-free *S. putrefaciens* incubations augmented with both calcium and magnesium, we observed 5-50  $\mu\text{m}$  calcium carbonate precipitates alongside well-defined, nano-botryoidal iron-rich clusters. These experiments yielded a broad range of carbonate mineral morphology, as shown in Figure 6 A-C. We observed both calcite and aragonite calcium carbonate polymorphs in the Raman scans of the combined cation experiment (Fig. 6G) that were undetected by bulk



XRD measurements (Fig. 2). TEM imaging of smaller precipitates revealed nano-scale iron-rich rods (Fig. 6D). HRTEM of these rods indicated a d-value of  $\sim 2.7 \text{ \AA}$  corresponding to the (301) reflection of goethite (Fig. 6E). TEM-EDS maps also showed minerals rich in iron (26 at. %), but depleted in both calcium and magnesium (<1 at. %) in the calcium- and magnesium-amended incubations (Fig. 6F).

In the presence of silica, the magnesium- and calcium-amended *S. putrefaciens* incubation produced even more complex carbonate morphologies. We detected 30 – 40  $\mu\text{m}$  calcium carbonate polymorphs, with <1 at.% incorporation of magnesium or iron, manifesting as bundles of outgrowing acicular needles branching out of a central plane (Fig. 6H), thick platy forms embedded in a siliceous matrix (Fig. 6I), porous, blunt-edge blades dusted with silica nanocolloids (Fig. 6J), and rhombohedral calcite (Fig. 6K). Raman analyses confirmed that these carbonate minerals were both aragonite and calcite (Fig. 6P), which was supported by bulk XRD analysis (Fig. 2). Additionally, HRTEM of stellate needles analyzed by FFT showed d-values (2.5, 3.4, and 4.7  $\text{\AA}$ ) consistent with aragonite (Fig. 6Q). TEM imaging showed a distinct separation of the carbonates from iron- and silica-rich phases (Fig. 6O), which instead formed friable aggregates (Fig. 6L,M,N). High magnification HAADF imaging of these aggregates demonstrated the platy, curling morphology of the nanostructures (Fig. 6L), rich in iron and silica (Fig. 6M), and comparable to the Fe-Si precipitates in the other silica-augmented conditions.

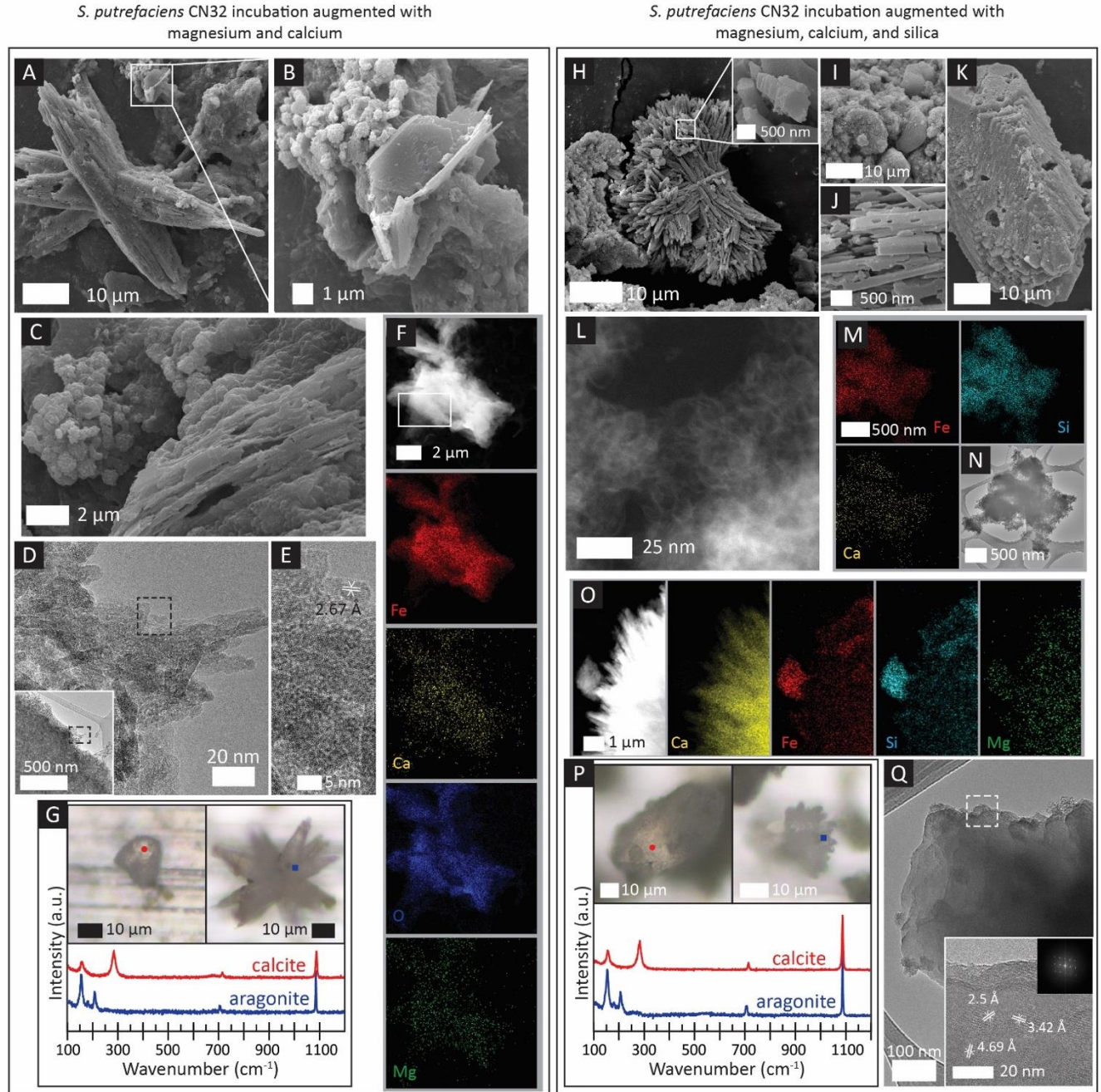


Figure 6: Characterization of biominerals formed in *S. putrefaciens* incubations amended with calcium and magnesium. SEM images of incubations without silica show carbonates (A,B), and spherical crust-like phases (C); TEM images of aggregates of rod-like phases, with a black rectangle designating the location of an HRTEM image (E) indicating *d*-value of goethite; HAADF and STEM-EDS mapping show iron-rich masses (red), deficient in calcium and magnesium; Raman spectra of different carbonate morphologies (G) indicate both calcite and aragonite minerals; in the presence of silica, minerals presented branching morphologies (H), globular blocks (I), perforated blades (J), and rhombohedral shapes (K) in SEM images; an HAADF image reveals clusters of wavy, friable phases (L) composed mainly of iron and silica (M), also shown in bright-field TEM (N); Raman measurements of calcite and aragonite Ca-carbonate polymorphs (P); HRTEM of an acicular mineral (Q) and FFT showing *d*-values consistent with aragonite (Q, subset).

## DISCUSSION

### Effect of dissolved silica and cations on microbial/dissimilatory iron reduction

#### *Silica*

In tandem, our ferrozine results and electron microscopy analyses suggest that silica sequesters ferrous iron into solid siliceous phases. In silica-free experiments, reduced Fe(II) increased in solution, while biogenic Fe(II) predominantly partitioned into solid precipitates under siliceous conditions. In silica-containing experiments, Fe(II)/T of averaged solids was approximately 25% higher than that in experiments without dissolved silica (Supplemental, Table 1). While the elevated Fe(II)/T ratios of solids (0.87 – 0.66) precipitating in silica-amended experiments could point to the formation of mixed-valence Fe-oxides (e.g., magnetite), we did not detect magnetite under these conditions by SEM- or TEM-based analyses, Raman spectroscopy, or XRD. Rather, we observed white-colored precipitates form over time, especially in the magnesium and magnesium-calcium incubations with dissolved silica (Fig. S5). Extensive clusters of amorphous friable, folding structures dominated the iron- and silica-rich phases in all bioreduction conditions (Fig. 3J, 4R, 5H,I, 6L,M,N). Thus, the formation of these siliceous phases likely incorporated much of the released Fe(II) in silica-bearing solutions.

Weak Fh reflections in SAED patterns of bioreduced iron-silica coprecipitates suggest that these Fe(II)-silica or Fe(II,III)-silica phases could precipitate on existing ferrihydrite surfaces or microbial surfaces embedded in the precipitate. The accumulations of iron- and silica-rich solid phases likely continue to ensnare Fe(II) released via microbial respiration within this aggregate. Microbially-induced microenvironments and microbe-mineral aggregates affect the extent of DIR and secondary mineralization (Fredrickson *et al.*, 1998; Zachara *et al.*, 2002; Zegeye *et al.*, 2010; Han *et al.*, 2018). For example, Zegeye *et al.* (2010) reported the highest retention of Fe(II) in dense geometries of microbe-mineral aggregates of *S. putrefaciens* and  $\gamma$ -FeOOH (Zegeye *et al.*, 2010). Indeed, *S. putrefaciens* biofilms that developed in the AAS-only experiments—and more extensively in the silica-amended condition—also appeared to sequester Fe(II), as indicated by our EDS observations and high Fe(II) in AAS solids (Fig. 1). SEM images of these samples indicated a close association with biomass and accumulations of iron-rich minerals (Fig. 2A,B). The presence of readily-precipitating silica likely amplifies the effects of Fe(II) retention in our experiments. The amassed biomineral aggregates in silica-amended experiments could also limit the diffusion of ferrous iron from the solid phase, similar to observations made by Pallud *et al.*, (2010) on the accumulation of Fe(II) and bicarbonate in interior regions of artificial soil aggregates inoculated with *S. putrefaciens*. Siliceous conditions could also enhance FeOOH mineral and microbial flocculation, as observed by Zachara *et al.*, (2002). Hence, restricted diffusion from the dense architecture of silica-rich solids in these incubations could also explain the depletion of Fe(II) in the silica-amended solutions.

The pivotal effect of silica on iron partitioning in the *S. putrefaciens* incubations was not evident in our abiotic control experiments, which remained as ferrihydrite (Fig. S3) after more than four months of incubation. We found no significant difference in the ferrous-ferric component in control solutions with or without silica. STEM-EDS maps of the control solid indicated silica adsorption to iron precipitates containing 8 at. % iron and 12 at. % silica. The consistency in Ferrozine measurements of the controls underscores how secondary iron mineral phases are dictated by both Fe(III) respiration, producing Fe(II), and the presence of dissolved silica.

### *Divalent Cation constituents*

Calcium and magnesium play a significant role in regulating cellular processes, including membrane transport and gene expression (Dominguez, 2004). Thus, as expected, the incorporation or exclusion of calcium and/or magnesium in experimental medium resulted in significant differences in mineral precipitates and aqueous iron concentrations. After 19 weeks of DIR performed by *S. putrefaciens*, we observed the highest concentrations of aqueous Fe(II) solutions amended with 10 mM Ca<sup>2+</sup> and similarly high dissolved ferrous iron concentrations in the combined cation solutions (Fig. 1). Ca-related complexation, adsorption, or calcium-associated metabolic pathways may promote these elevated aqueous Fe(II) levels, either through enhancing reduction and/or promoting the presence of soluble rather than precipitated Fe(II). Alternatively, calcium's effect on the behavior of Fe(II) may relate to microbe-mineral aggregation. A previous study found that anaerobic growth conditions triggered disaggregation in *Shewanella oneidensis* MR1 cultures supplemented with 0.68 mM Ca<sup>2+</sup> (McLean *et al.*, 2008). If calcium limited cellular aggregation in our anaerobic Fe(III) respiration experiments, then the iron-silica adsorptive shielding effect proposed earlier may not have developed as extensively, allowing more Fe(II) to escape into solution.

### **Secondary mineral products**

#### *Carbonates*

The most obvious effect of adding calcium was in the production of calcium carbonate polymorphs, which formed in both *S. putrefaciens* incubations and control experiments. Despite its lower thermodynamic stability, aragonite precipitation is favored over calcite in the presence of Fe(II) and Mg(II) (Zeller, E.J., Wray, 1956; Berner, 1975; Mucci & Morse, 1982). Fe(II) inhibits normal calcite spiral growth (Di Lorenzo *et al.*, 2017) and the incorporation of Mg(II) into the calcite lattice either increases surface energy (Sun *et al.*, 2015b) or increases calcite solubility (Davis *et al.*, 2000). Raman spectral scans at a microscale expanded on the more limited bulk XRD analyses and confirmed the stark morphological differences seen in SEM imaging.

We observed both aragonite and calcite polymorphs in *S. putrefaciens* incubations modified with magnesium, calcium, and both divalent cations, signaling the intricacies of polymorph selection in complex biological solutions. Despite conditions favorable for aragonite precipitation, including a biomineralizing environment and supplemented magnesium, the [Mg]/[Ca] ratio in our experiments remains lower than the critical limit established for aragonite selection (i.e., [Mg]/[Ca] ≥ 2) (Sun *et al.*, 2015b), supporting our observations of both polymorphs. In calcium-amended conditions with *S. putrefaciens*, initial calcite precipitation was likely overtaken by aragonite mineralization due to the increasing ferrous iron and/or an EPS matrix. In contrast, we identified only calcite and no aragonite in Raman scans of minerals in Ca-amended abiotic controls, further clarifying the role for cellular organics, biogenic Fe(II), and Mg<sup>2+</sup> in aragonite precipitation.

Dissolved silica could also play a role in carbonate crystal growth or polymorphism in the bioreduction incubations with *S. putrefaciens*. Kellermeier *et al.* (2013) observed both the stabilizing effects of surface-adsorbed silica on metastable CaCO<sub>3</sub> polymorphs and also silica-enhanced calcite growth low temperatures in a study on the transformation of CaCO<sub>3</sub> polymorphism with increasing temperature and silica concentration. Unlike silica-free

experiments that contained large, more singular calcium carbonate crystals, we frequently observed smaller individual needles and blades fusing into larger mineral aggregates in Si-amended experiments (e.g., Fig. 6); however, the exact role of dissolved silica in carbonate morphology is difficult to quantify in these experiments.

Iron carbonates, including siderite, were not detected in these experimental conditions. This dearth of Fe-carbonates could be attributed to low Fe-concentrations relative to concentrations of the calcium- and magnesium cations.

### *Goethite*

We identified secondary Fe(III) phases including goethite ( $\alpha$ -FeOOH) and 6-line ferrihydrite in silica-free *S. putrefaciens* incubations, confirming Ferrozine results that indicated there was only partial reduction of the starting ferrihydrite substrate. This partial reduction occurred irrespective of the availability of excess electron donor (lactate) for *S. putrefaciens*. Secondary goethite mineralization arising from the microbial respiration of ferrihydrite is well documented (Fredrickson *et al.*, 2001, 2003; Hansel *et al.*, 2003; Pallud *et al.*, 2010; Bae & Lee, 2013; Han *et al.*, 2018). This secondary  $\alpha$ -FeOOH mineralizes through dissolution and re-precipitation transformations of ferrihydrite during reactions with Fe(II), where sorbed Fe(II) passivates the ferrihydrite surface at low initial Fe(II) concentrations (<0.3 mM), inducing the mineralization of goethite instead of magnetite (Hansel *et al.*, 2003). After our 19 week incubations, the bioreduced solutions without silica had a mean [Fe(II)] of 0.34 mM (Fig. 1/Table 1). Since the initial Fe(II) concentration was probably similar to control experiments (0.03 mM), increasing over time during bioreduction, goethite plausibly formed through this reductive dissolution pathway. In addition, we found further evidence of partial Fe(III) reduction with the tentative identification of 6LFh alongside goethite in silica-free experiments indicates there was an increase in particle size and crystallinity of the starting ferrihydrite substrate during microbial Fe(III) respiration.

In contrast, experiments augmented with silica did not form goethite. One reason for this lack of goethite could be that silica stabilizes non-crystalline ferrihydrite by blocking sorption of Fe(II) at reactive sites on the mineral surface (Schwertmann & Thalmann, 1976; Jones *et al.*, 2009), subsequently hindering its transformation to other Fe-oxides (Anderson & Benjamin, 1985; Lee & Xu, 2019). Alternatively, our results suggest that released Fe(II) bonded with silica to form iron-silica coprecipitates (Fig. 1). Perhaps the silica enclosing ‘captured’ Fe(II) in these coprecipitates then limits subsequent Fe(II) interaction with remnant ferrihydrite. Regardless of whether one or both of these possible mechanisms took place, the absence of goethite in our siliceous incubations suggests that the dissolved silica component prevented Fe(II)-induced solid state transformation to other Fe oxides (e.g., goethite, magnetite, hematite).

### *Proto-silicates*

In our incubations amended with dissolved silica, we observe the formation of novel iron-silica coprecipitates. These iron- and silica-rich precipitates lack definitive crystal structure, yielding diffuse rings in SAED patterns albeit often bearing weak 2LFh reflections, and no resolvable lattice fringe in HRTEM to ascertain their d-spacing. While their electron diffraction patterns are suggestive of two-line ferrihydrite, the iron-silica coprecipitates are morphologically distinct from their antecedent ferrihydrite minerals, which are composed of pseudo-hexagonal crystallites (Fig. S3). In contrast, the iron-silica phase is characterized by thin, curling, and folding layers as well as high Fe, Si, and O. Furthermore, the high Fe(II)/T of the silica-amended

bio-reduced solids, unlike the silica-lacking experiments, implies that these curled phases are Fe(II)-rich. Therefore, we suggest that these structures are incipient Fe(II)-rich silicates.

As these iron-silica curling precipitates are absent in silica-amended control products, we propose that bacterially-catalyzed Fe(II) is essential to the formation of these phases. Similar structures were observed by Hinz *et al.* (2021) in low temperature abiotic reactions of Fe(II)/Fe(III) mixtures at circumneutral pH in artificial Archean seawater, further supporting the hypothesis that Fe(II) is critical for forming proto-iron silicates. In our experiments where iron was introduced solely as Fe(III), biogenic production of Fe(II) from DIR was required to produce these putative precursor iron silicates.

## Implications for Precambrian BIFs

Microbial Fe(III) respiration likely mediated BIF deposition and early stages of diagenesis (Walker, 1984; Konhauser *et al.*, 2005). One proposed mechanism for BIF formation argues for the deposition of primary iron oxides (e.g., ferrihydrite) (LaBerge, 1964; Beukes *et al.*, 2008; Konhauser *et al.*, 2017) that transformed into iron silicates, carbonates, magnetite, or other phases during iron bioreduction hosted in ancient sediments (Fischer & Knoll, 2009). We tested this hypothesis using laboratory simulations of *S. putrefaciens* suspensions in artificial Archean seawater to examine microbial iron reduction as a viable pathway for ancient iron silicate formation.

The minerals produced in our DIR incubations and control solutions are distinct from the early BIF assemblage and other Precambrian laboratory studies. We observed pervasive calcium carbonate precipitation, and no evidence of iron carbonates—siderite or ankerite—that are ubiquitous in the BIF record (Trendall, 2002; Klein, 2005) and often attributed to dissimilatory iron reduction (Mozley & Carothers, 1992; Zeng & Tice, 2014). Reports of calcium-rich siderite in similar Fe bioreduction incubations (Zeng & Tice, 2014) did not recur in our experimental setup. As we addressed the typical omission of calcium ions by adding  $\text{Ca}^{2+}$  at concentrations estimated for Archean oceans (Holland, 1984), we solely observed the precipitation of calcium carbonates in our experiments instead of iron carbonates. We suggest that  $\text{CaCO}_3$  dominated due to a low  $[\text{Fe}]/[\text{Ca}]$  and low total  $[\text{Fe}]$ , incompatible with the likely higher  $[\text{Fe(III)}]$  concentrations of iron oxides or Fe-silica matrix in an ancient sedimentary package. Hence, our experimental results are more suitable for examining the mineral products from microbial iron respiration in an environment mimicking the shallow water column with dilute Fe(III) oxides. Moreover, based on calcium estimates in the Archean ocean ( $[\text{Ca}] \sim 10 \text{ mM}$ ) and the proliferate calcium carbonates in these bioreduction incubations, we would expect to find calcium carbonates in the BIF record. It is possible that initial  $\text{CaCO}_3$  minerals could have transformed into ankerite, dolomite, siderite, and other BIF accessory minerals through interactions with diagenetic fluids (Zeng & Tice, 2014). Alternatively, our results may imply that the Archean ocean was actually less saturated with respect to calcium carbonate than previously predicted. Another plausible explanation could constrain BIF depositional environments to below the carbonate compensation depth (CCD).

Finally, our results demonstrate the precipitation of potential Fe(II)-rich proto-silicates in incubations with *S. putrefaciens*. However, even with a surplus of electron donor (lactate) and conditions apt for comprehensive Fe(III) respiration, we still observed substantial Fe(III) remaining in solids, with 0.13 – 0.34 Fe(III)/T in experiments amended with silica and 0.31 – 0.47 Fe(III)/T in silica-free conditions. Given the Fe(III) composition of the experimental solids, our findings suggest initial iron oxides would be preserved in the BIF record. In fact, early nano-

inclusions of hematite reported by Sun *et al.* (2015a) and Li *et al.* (2013a) 2.5 Ga Hamersley Group BIFs could be relicts of a primary ferric oxyhydroxide. In contrast, (Rasmussen *et al.*, 2016, 2021) argue that these nano-scale ferric oxide dusts are secondary to primary Fe(II) silicates (i.e., greenalite) based on textural relationships and paleomagnetic evidence, suggesting iron oxides in BIFs formed during later stage fluid-rock interactions, metamorphism, and/or oxidative weathering (Rasmussen *et al.*, 2013, 2016, 2019, 2021; Muhling & Rasmussen, 2020). We were unable to test the full extent of bioreduction requisite for microbially-mediated ferrous silicate mud precursors in BIFs given our remnant Fe(III), nutrient-depleted medium (e.g. phosphate and potentially other trace elements), and time limitations of our 19-week bioreduction incubations. However, investigating microbial Fe(III) respiration on more substantial timescales or with continuous chemostat cultures could result in the complete reduction of ferrihydrite and sole production of Fe(II)-rich proto-silicates. While it is impossible to truly replicate Archean sedimentary porewaters in modern laboratory reconstructions, our experiments simulating microbial Fe(III) oxide respiration in a silica-rich seawater environment demonstrate that incipient iron silicates may also have formed from DIR of early ferric substrates, suggesting an alternative genesis for early BIF iron silicates.

## REFERENCES

- Anderson PR, Benjamin MM (1985) Effects of Silicon on the Crystallization and Adsorption Properties of Ferric Oxides. *Environmental Science and Technology* **19**, 1048–1053.
- Bae S, Lee W (2013) Biotransformation of lepidocrocite in the presence of quinones and flavins. *Geochimica et Cosmochimica Acta* **114**, 144–155.
- Balch WE, Wolfe RS (1976) New approach to the cultivation of methanogenic bacteria: 2 mercaptoethanesulfonic acid (HS CoM) dependent growth of *Methanobacterium ruminantium* in a pressurized atmosphere. *Applied and Environmental Microbiology* **32**, 781–791.
- Baur ME, Hayes JM, Studley SA, Walter MR (1985) Millimeter-scale variations of stable isotope abundances in carbonates from Banded Iron-Formations in the Hamersley Group of Western Australia. *Economic Geology* **80**, 270–282.
- Bekker A, Krapež B, Slack JF, Planavsky N, Hofmann A, Konhauser KO, Rouxel OJ (2010) Iron formation: The sedimentary product of a complex interplay among mantle, tectonic, oceanic, and biospheric processes—a reply. *Economic Geology* **107**, 379–380.
- Bekker A, Planavsky NJ, Krapež B, Rasmussen B, Hofmann A, Slack JF, Rouxel OJ, Konhauser KO (2013) *Iron Formations: Their Origins and Implications for Ancient Seawater Chemistry. Treatise on Geochemistry: Second Edition*, 2nd edn. Elsevier Ltd.
- Berner RA (1975) The role of magnesium in the crystal growth of calcite and aragonite from sea water. *Geochimica et Cosmochimica Acta* **39**.
- Beukes NJ, Mukhopadhyay J, Gutzmer J (2008) Genesis of high-grade iron ores of the Archean

- Iron Ore Group around Noamundi, India. *Economic Geology* **103**, 365–386.
- Craddock PR, Dauphas N (2011) Iron and carbon isotope evidence for microbial iron respiration throughout the Archean. *Earth and Planetary Science Letters* **303**, 121–132.
- Davis KJ, Dove PM, Yoreo JJ De (2000) The role of Mg<sup>2+</sup> as an impurity in calcite growth. *Science* **290**, 1134–1137.
- Dominguez DC (2004) Calcium signalling in bacteria. *Molecular Microbiology* **54**, 291–297.
- Dong H, Jaisi DP, Kim J, Zhang G (2009) Microbe-clay mineral interactions. *American Mineralogist* **94**, 1505–1519.
- Etique M, Jorand FPA, Ruby C (2016) Magnetite as a precursor for green rust through the hydrogenotrophic activity of the iron-reducing bacteria *Shewanella putrefaciens*. *Geobiology* **14**, 237–254.
- Farquhar J, Nanping WU, Canfield DE, Oduro H (2010) Connections between sulfur cycle evolution, sulfur isotopes, sediments and base metal sulfide deposits. *Economic Geology* **105**, 509–533.
- Fischer WW, Knoll AH (2009) An iron shuttle for deepwater silica in late Archean and early Paleoproterozoic iron formation. *Bulletin of the Geological Society of America* **121**, 222–235.
- Fredrickson JK, Kota S, Kukkadapu RK, Liu C, Zachara JM (2003) Influence of electron donor/acceptor concentrations on hydrous ferric oxide (HFO) bioreduction. *Biodegradation* **14**, 91–103.
- Fredrickson JK, Zachara JM, Kennedy DW, Dong H, Onstott TC, Hinman NW, Li SM (1998) Biogenic iron mineralization accompanying the dissimilatory reduction of hydrous ferric oxide by a groundwater bacterium. *Geochimica et Cosmochimica Acta* **62**, 3239–3257.
- Fredrickson JK, Zachara JM, Kukkadapu RK, Gorby YA, Smith SC, Brown CF (2001) Biotransformation of Ni-substituted hydrous ferric oxide by an Fe(III)-reducing bacterium. *Environmental Science and Technology* **35**, 703–712.
- Furukawa Y, Reilly SEO (2007) Rapid precipitation of amorphous silica in experimental systems with nontronite (NAu-1) and *Shewanella oneidensis* MR-1. *Geochimica et Cosmochimica Acta* **71**, 363–377.
- Gorby YA, Yanina S, Mclean JS, Rosso KM, Moyles D, Dohnalkova A, Beveridge TJ, Chang IS, Kim BH, Kim KS, Culley DE, Reed SB, Romine MF, Saffarini DA, Hill EA, Shi L, Elias DA, Kennedy DW, Pinchuk G, Watanabe K, Ishii S, Logan B, Nealson KH, Fredrickson JK (2006) Electrically conductive bacterial nanowires produced by *Shewanella oneidensis* strain MR-1 and other microorganisms **103**.



- Halevy I, Bachan A (2017) The geologic history of seawater pH. *Science* **355**, 1069–1071.
- Han R, Liu T, Li F, Li X, Chen D, Wu Y (2018) Dependence of Secondary Mineral Formation on Fe(II) Production from Ferrihydrite Reduction by *Shewanella oneidensis* MR-1. *ACS Earth and Space Chemistry* **2**, 399–409.
- Hansel CM, Benner SG, Neiss J, Dohnalkova A, Kukkadapu RK, Fendorf S (2003) Secondary mineralization pathways induced by dissimilatory iron reduction of ferrihydrite under advective flow. *Geochimica et Cosmochimica Acta* **67**, 2977–2992.
- Heimann A, Johnson CM, Beard BL, Valley JW, Roden EE, Spicuzza MJ, Beukes NJ (2010) Fe, C, and O isotope compositions of banded iron formation carbonates demonstrate a major role for dissimilatory iron reduction in ~2.5Ga marine environments. *Earth and Planetary Science Letters* **294**, 8–18.
- Higgins JA, Fischer WW, Schrag DP (2009) Oxygenation of the ocean and sediments: Consequences for the seafloor carbonate factory. *Earth and Planetary Science Letters* **284**, 25–33.
- Hinz IL, Nims C, Theuer S, Templeton AS, Johnson JE (2021) Ferric iron triggers greenalite formation in simulated Archean seawater. *Geology* **XX**, 1–6.
- Holland HD (1984) *The Chemical Evolution of the Atmosphere and Ocean*. Princeton University Press.
- Janney DE, Cowley JM, Buseck PR (2000) Transmission electron microscopy of synthetic 2- and 6-line ferrihydrite. *Clays and Clay Minerals* **48**, 111–119.
- Johnson CM, Beard BL, Roden EE (2008) The iron isotope fingerprints of redox and biogeochemical cycling in modern and ancient earth. *Annual Review of Earth and Planetary Sciences* **36**, 457–493.
- Johnson CM, Ludois JM, Beard BL, Beukes NJ, Heimann A (2013) Iron formation carbonates: Paleooceanographic proxy or recorder of microbial diagenesis? *Geology* **41**, 1147–1150.
- Johnson JE (2019) From minerals to metabolisms: Evidence for life before oxygen from the geological record. *Free Radical Biology and Medicine* 0–1.
- Johnson JE, Molnar PH (2019) Widespread and Persistent Deposition of Iron Formations for Two Billion Years. *Geophysical Research Letters* **46**, 3327–3339.
- Johnson JE, Muhling JR, Cosmidis J, Rasmussen B, Templeton AS (2018) Low-Fe(III) Greenalite Was a Primary Mineral From Neoproterozoic Oceans. *Geophysical Research Letters* **45**, 3182–3192.
- Jones AM, Collins RN, Rose J, Waite TD (2009) The effect of silica and natural organic matter on the Fe(II)-catalysed transformation and reactivity of Fe(III) minerals. *Geochimica et*

*Cosmochimica Acta* **73**, 4409–4422.

Jones C, Nomosatryo S, Crowe SA, Bjerrum CJ, Canfield DE (2015) Iron oxides, divalent cations, silica, and the early earth phosphorus crisis. *Geology* **43**, 135–138.

Jorand, F ; Appenzeller, B. M. R ; Abdelmoula, M ; Refait, P ; Block, J.C ; Genin J-MR (2000) Assessment of vivianite formation in *Shewanella putrefaciens* culture. *Environmental Technology* **21**.

Kato S, Itoh T, Yuki M, Nagamori M, Ohnishi M, Uematsu K, Suzuki K, Takashina T, Ohkuma M (2019) Isolation and characterization of a thermophilic sulfur- and iron-reducing thaumarchaeote from a terrestrial acidic hot spring. *ISME Journal* **13**, 2465–2474.

Kellermeier M, Glaab F, Klein R, Melero-García E, Kunz W, García-Ruiz JM (2013) The effect of silica on polymorphic precipitation of calcium carbonate: An on-line energy-dispersive X-ray diffraction (EDXRD) study. *Nanoscale* **5**, 7054–7065.

Klein C (2005) Some Precambrian banded iron-formations (BIFs) from around the world: Their age, geologic setting, mineralogy, metamorphism, geochemistry, and origin. *American Mineralogist* **90**, 1473–1499.

Knoll AH, Bergmann KD, Strauss J V. (2016) Life: The first two billion years. *Philosophical Transactions of the Royal Society B: Biological Sciences* **371**.

Komlos J, Kukkadapu RK, Zachara JM, Jaffé PR (2007) Biostimulation of iron reduction and subsequent oxidation of sediment containing Fe-silicates and Fe-oxides: Effect of redox cycling on Fe(III) bioreduction. *Water Research* **41**, 2996–3004.

Konhauser KO, Amskold L, Lalonde S V., Posth NR, Kappler A, Anbar A (2007) Decoupling photochemical Fe(II) oxidation from shallow-water BIF deposition. *Earth and Planetary Science Letters* **258**, 87–100.

Konhauser KO, Newman DK, Kappler a. (2005) The potential significance of microbial Fe (III) reduction. *Geobiology* **3**, 167–177.

Konhauser KO, Planavsky NJ, Hardisty DS, Robbins LJ, Warchola TJ, Hugaard R, Lalonde S V., Partin CA, Oonk PBH, Tsikos H, Lyons TW, Bekker A, Johnson CM (2017) Iron formations: A global record of Neoproterozoic to Palaeoproterozoic environmental history. *Earth-Science Reviews* **172**, 140–177.

Koo TH, Lee G, Kim JW (2016) Biogeochemical dissolution of nontronite by *Shewanella oneidensis* MR-1: Evidence of biotic illite formation. *Applied Clay Science* **134**, 13–18.

Kostka JE, Haefele E, Viehweger R, Stucki JW (1999) Respiration and dissolution of iron(III)-containing clay minerals by bacteria. *Environmental Science and Technology* **33**, 3127–3133.

- Kostka JE, Stucki JW, Nealson KH, Jun WU (1996) Reduction of structural Fe(III) in smectite by a pure culture of *Shewanella putrefaciens* strain MR-1. *Clays and Clay Minerals* **44**, 522–529.
- Krapež B, Barley ME, Pickard AL (2003) Hydrothermal and resedimented origins of the precursor sediments to banded iron formation: Sedimentological evidence from the Early Palaeoproterozoic Brockman Supersequence of Western Australia. *Sedimentology* **50**, 979–1011.
- Krissansen-Totton J, Arney GN, Catling DC (2018) Constraining the climate and ocean pH of the early Earth with a geological carbon cycle model. *Proceedings of the National Academy of Sciences of the United States of America* **115**, 4105–4110.
- Kukkadapu RK, Zachara JM, Fredrickson JK, Kennedy DW (2004) Biotransformation of two-line silica-ferrihydrite by a dissimilatory Fe(III)-reducing bacterium: Formation of carbonate green rust in the presence of phosphate. *Geochimica et Cosmochimica Acta* **68**, 2799–2814.
- LaBerge G (1964) Development of magnetite in iron formations of the Lake superior region. *Economic Geology*.
- Langley S, Gault A, Ibrahim A, Renaud R, Fortin D, Clark ID, Ferris FG (2009) A comparison of the rates of Fe(III) reduction in synthetic and bacteriogenic iron oxides by *Shewanella putrefaciens* CN32. *Geomicrobiology Journal* **26**, 57–70.
- Lee S, Xu H (2019) One-Step Route Synthesis of Siliceous Six-Line Ferrihydrite: Implication for the Formation of Natural Ferrihydrite. *ACS Earth and Space Chemistry* **3**, 503–509.
- Li YL, Cole DR, Konhauser K, Chan LS (2013a) Quartz nanocrystals in the 2.48 Ga Dales Gorge banded iron formation of Hamersley, Western Australia: Evidence for a change from submarine to subaerial volcanism at the end of the Archean. *American Mineralogist* **98**, 582–587.
- Li YL, Konhauser KO, Kappler A, Hao XL (2013b) Experimental low-grade alteration of biogenic magnetite indicates microbial involvement in generation of banded iron formations. *Earth and Planetary Science Letters* **361**, 229–237.
- Lorenzo F Di, Burgos-Cara A, Ruiz-Agudo E, Putnis C V., Prieto M (2017) Effect of ferrous iron on the nucleation and growth of CaCO<sub>3</sub> in slightly basic aqueous solutions. *CrystEngComm* **19**, 447–460.
- Maliva RG, Knoll AH, Simonson BM (2005) Secular change in the Precambrian silica cycle: Insights from chert petrology. *Bulletin of the Geological Society of America*.
- McLean JS, Pinchuk GE, Geydebrekht O V., Bilskis CL, Zakrajsek BA, Hill EA, Saffarini DA, Romine MF, Gorby YA, Fredrickson JK, Beliaev AS (2008) Oxygen-dependent autoaggregation in *Shewanella oneidensis* MR-1. *Environmental Microbiology* **10**, 1861–1876.
- Miot J, Etique M (2016) Formation and Transformation of Iron-Bearing Minerals by Iron(II)-

Oxidizing and Iron(III)-Reducing Bacteria. *Iron Oxides: From Nature to Applications* 53–97.

Mozley PS, Carothers WW (1992) Elemental and isotopic composition of siderite in the Kuparuk Formation, Alaska: effect of microbial activity and water/sediment interaction on early pore-water chemistry. *Journal of Sedimentary Petrology* **62**, 681–692.

Mucci A, Morse JW (1982) The incorporation of divalent Mg and divalent Sr into calcite overgrowths : influences of growth rate and solution composition. *Geochimica et Cosmochimica Acta* **47**, 217–233.

Muhling JR, Rasmussen B (2020) Widespread deposition of greenalite to form Banded Iron Formations before the Great Oxidation Event. *Precambrian Research* **339**, 105619.

Myers CR, Nealson KH (1990) Respiration-linked proton translocation couples to anaerobic reduction of manganese(IV) and iron(III) in *Shewanella putrefaciens* MR-1. *Journal of Bacteriology* **172**, 6232–6238.

O’Loughlin EJ, Gorski CA, Flynn TM, Scherer MM (2019) Electron donor utilization and secondary mineral formation during the bioreduction of lepidocrocite by *shewanella putrefaciens* CN32. *Minerals* **9**.

O’Loughlin EJ, Larese-Casanova P, Scherer M, Cook R (2007) Green rust formation from the bioreduction of  $\gamma$ -FeOOH (Lepidocrocite): Comparison of several *Shewanella* species. *Geomicrobiology Journal* **24**, 211–230.

O’Reilly SE (2005) Secondary mineral formation associated with respiration of nontronite, N Au-1 by iron reducing bacteria. *Geochemical Transactions* **6**, 67.

Pakchung AAH, Soe CZ, Codd R (2008) Studies of iron-uptake mechanisms in two bacterial species of the *Shewanella* genus adapted to middle-range (*Shewanella putrefaciens*) or Antarctic (*Shewanella gelidimarina*) temperatures. *Chemistry and Biodiversity* **5**, 2113–2123.

Pallud C, Masue-Slowey Y, Fendorf S (2010) Aggregate-scale spatial heterogeneity in reductive transformation of ferrihydrite resulting from coupled biogeochemical and physical processes. *Geochimica et Cosmochimica Acta* **74**, 2811–2825.

Percak-Dennet EM, Beard BL, Xu H, Konishi H, Johnson CM, Roden EE (2011) Iron isotope fractionation during microbial dissimilatory iron oxide reduction in simulated Archaean seawater. *Geobiology* 205–220.

Peretyazhko TS, Zachara JM, Kennedy DW, Fredrickson JK, Arey BW, McKinley JP, Wang CM, Dohnalkova AC, Xia Y (2010) Ferrous phosphate surface precipitates resulting from the reduction of intragrain 6-line ferrihydrite by *Shewanella oneidensis* MR-1. *Geochimica et Cosmochimica Acta* **74**, 3751–3767.

Phoenix VR, Konhauser KO, Ferris FG (2003) Experimental study of iron and silica

immobilization by bacteria in mixed Fe-Si systems: Implications for microbial silicification in hot springs. *Canadian Journal of Earth Sciences* **40**, 1669–1678.

Piepenbrock A, Dippon U, Porsch K, Appel E, Kappler A (2011) Dependence of microbial magnetite formation on humic substance and ferrihydrite concentrations. *Geochimica et Cosmochimica Acta* **75**, 6844–6858.

Poulton SW, Canfeld DE (2011) Ferruginous conditions: A dominant feature of the ocean through Earth's history. *Elements* **7**, 107–112.

Rasmussen B, Krapež B, Meier DB (2014) Replacement origin for hematite in 2.5 Ga banded iron formation: Evidence for postdepositional oxidation of iron-bearing minerals. *Bulletin of the Geological Society of America* **126**, 438–446.

Rasmussen B, Krapež B, Muhling JR (2015a) Seafloor silicification and hardground development during deposition of 2.5 Ga banded iron formations. *Geology* **43**, 235–238.

Rasmussen B, Krapež B, Muhling JR, Suvorova A (2015b) Precipitation of iron silicate nanoparticles in early Precambrian oceans marks Earth's first iron age 303–306.

Rasmussen B, Meier DB, Krapež B, Muhling JR (2013) Iron silicate microgranules as precursor sediments to 2.5-billion-year-old banded iron formations. *Geology* **41**, 435–438.

Rasmussen B, Muhling JR, Fischer WW (2019) Evidence from laminated chert in banded iron formations for deposition by gravitational settling of iron-silicate muds. *Geology* **47**, 167–170.

Rasmussen B, Muhling JR, Krapež B (2021) Greenalite and its role in the genesis of early Precambrian iron formations – A review. *Earth-Science Reviews* **217**.

Rasmussen B, Muhling JR, Suvorova A, Krapež B (2016) Dust to dust: Evidence for the formation of “primary” hematite dust in banded iron formations via oxidation of iron silicate nanoparticles. *Precambrian Research* **284**, 49–63.

Reddy TR, Zheng XY, Roden EE, Beard BL, Johnson CM (2016) Silicon isotope fractionation during microbial reduction of Fe(III)–Si gels under Archean seawater conditions and implications for iron formation genesis. *Geochimica et Cosmochimica Acta* **190**, 85–99.

Robbins LJ, Funk SP, Flynn SL, Warchola TJ, Li Z, Lalonde S V., Rostron BJ, Smith AJB, Beukes NJ, Kock MO de, Heaman LM, Alessi DS, Konhauser KO (2019) Hydrogeological constraints on the formation of Palaeoproterozoic banded iron formations. *Nature Geoscience* **12**, 558–563.

Salas EC, Berelson WM, Hammond DE, Kampf AR, Nealson KH (2009) The influence of carbon source on the products of dissimilatory iron reduction. *Geomicrobiology Journal* **26**, 451–462.

- Salas EC, Berelson WM, Hammond DE, Kampf AR, Nealson KH (2010) The impact of bacterial strain on the products of dissimilatory iron reduction. *Geochimica et Cosmochimica Acta* **74**, 574–583.
- Schwertmann U, Thalmann H (1976) The Influence of [Fe(II)], [Si], and pH on the formation of lepidocrocite and ferrihydrite during oxidation of aqueous FeCl<sub>2</sub> solutions. *Clay Minerals* **11**, 189–200.
- Sergent AS, Jorand F, Hanna K (2011) Effects of Si-bearing minerals on the nature of secondary iron mineral products from lepidocrocite bioreduction. *Chemical Geology* **289**, 86–97.
- Siever R (1992) The silica cycle in the Precambrian. *Geochimica et Cosmochimica Acta* **56**, 3265–3272.
- Sklute EC, Kashyap S, Dyar MD, Holden JF, Tague T, Wang P, Jaret SJ (2018) Spectral and morphological characteristics of synthetic nanophase iron (oxyhydr)oxides. *Physics and Chemistry of Minerals* **45**, 1–26.
- Stookey LL (1970) Ferrozine-A New Spectrophotometric Reagent for Iron. *Analytical Chemistry* **42**, 779–781.
- Stucki JW, Kostka JE (2006) Microbial reduction of iron in smectite. *Comptes Rendus - Geoscience* **338**, 468–475.
- Suirvey USG, Resourirces W, River P, Myers R (1988) Lovley, Phillips - 1988 - Novel mode of microbial energy metabolism organic carbon oxidation coupled to dissimilatory reduction of iron **54**, 1472–1480.
- Sun S, Konhauser KO, Kappler A, Li YL (2015a) Primary hematite in Neoproterozoic to Paleoproterozoic oceans. *Bulletin of the Geological Society of America* **127**, 850–861.
- Sun W, Jayaraman S, Chen W, Persson KA, Ceder G (2015b) Correction: Nucleation of metastable aragonite CaCO<sub>3</sub> in seawater (Proceedings of the National Academy of Sciences of the United States of America (2015), 112:3199-3204 (DOI: 10.1073/pnas.1423898112)). *Proceedings of the National Academy of Sciences of the United States of America* **112**, E2735.
- Tosca NJ, Jiang CZ, Rasmussen B, Muhling J (2019) Products of the iron cycle on the early Earth. *Free Radical Biology and Medicine* **140**, 138–153.
- Trendall AF (2002) *The significance of iron-formation in the Precambrian stratigraphic record*.
- Viollier E, Inglett PW, Hunter K, Roychoudhury AN, Cappellen P Van (2000) The Ferrozine method revisited. *Applied Geochemistry* **15**, 785–790.
- Walker JCG (1984) Suboxic diagenesis in banded iron formations. *Nature* **309**, 340–342.
- Widdel F, Kohring G-W, Mayer F (1983) Studies on dissimilatory sulfate-reducing bacteria that decompose fatty acids. *Archives of Microbiology* **134**, 286–294.
- Wu L, Beard BL, Roden EE, Johnson CM (2009) Influence of pH and dissolved Si on Fe isotope

fractionation during dissimilatory microbial reduction of hematite. *Geochimica et Cosmochimica Acta* **73**, 5584–5599.

Yahaya S, Aisha B., Zegeye A, Manning DAC, Fialips C. (2019) Biobleaching of silica sand using bioreducing bacteria (*Shewanella* strains). *Bayero Journal of Pure and Applied Sciences* **11**, 93.

Zachara JM, Kukkadapu RK, Fredrickson JK, Gorby YA, Smith SC (2002) Biomineralization of poorly crystalline Fe(III) oxides by dissimilatory metal reducing bacteria (DMRB). *Geomicrobiology Journal* **19**, 179–207.

Zachara JM, Kukkadapu RK, Peretyazhko T, Bowden M, Wang C, Kennedy DW, Moore D, Arey B (2011) The mineralogic transformation of ferrihydrite induced by heterogeneous reaction with bioreduced anthraquinone disulfonate (AQDS) and the role of phosphate. *Geochimica et Cosmochimica Acta* **75**, 6330–6349.

Zegeye A, Mustin C, Jorand F (2010) Bacterial and iron oxide aggregates mediate secondary iron mineral formation: Green rust versus magnetite. *Geobiology* **8**, 209–222.

Zegeye A, Ona-Nguema G, Carteret C, Huguet L, Abdelmoula M, Jorand F (2005) Formation of hydroxysulphate green rust 2 as a single iron(II-III) mineral in microbial culture. *Geomicrobiology Journal* **22**, 389–399.

Zeller, E.J., Wray J (1956) Factors Influencing Precipitation of Calcium Carbonate. *AAPG Bulletin* **40**, 140–152.

Zeng Z, Tice MM (2014) Promotion and nucleation of carbonate precipitation during microbial iron reduction. *Geobiology* **12**, 362–371.